LAWRENCE
LIVERMORE
NATIONAL
LABORATORY

National Ignition Facility Quarterly Report 2014

J. Kilkenny

December 29, 2014

Disclaimer

This document was prepared as an account of work sponsored by an agency of the United States government. Neither the United States government nor Lawrence Livermore National Security, LLC, nor any of their employees makes any warranty, expressed or implied, or assumes any legal liability or responsibility for the accuracy, completeness, or usefulness of any information, apparatus, product, or process disclosed, or represents that its use would not infringe privately owned rights. Reference herein to any specific commercial product, process, or service by trade name, trademark, manufacturer, or otherwise does not necessarily constitute or imply its endorsement, recommendation, or favoring by the United States government or Lawrence Livermore National Security, LLC. The views and opinions of authors expressed herein do not necessarily state or reflect those of the United States government or Lawrence Livermore National Security, LLC, and shall not be used for advertising or product endorsement purposes.

Table of Contents

Foreword

This is the second issue of Lawrence Livermore National Laboratory's National Ignition Facility (NIF) Quarterly Report. Our aim with this report is to deliver detailed technical reviews of NIF experiments, as well as updates on the science and technology underway to advance this world-class facility. This issue presents four articles, three of which discuss the production and performance of targets fielded on NIF, while the fourth details efforts to improve a key diagnostic at NIF.

The first article describes a novel process for removing micron-scale surface defects on NIF ignition capsules. These typically dome-shaped defects are an unintended consequence of micron-scale debris in the vapor-deposition process used to make the capsule. With the new method, an ultraviolet laser system is successfully used to reduce offending surface features to a size where they can be completely removed by tumble finishing. The result is an improvement in shell surface finish and increase in NIF capsule fabrication yield.

The second article describes the results of a campaign fielded on NIF to assess the potential advantages of rugby-shaped gold hohlraums for ignition experiments. The rugby capsule was predicted to have higher overall coupling efficiency of laser energy to x-ray drive and a comparable radiation temperature to conventional cylindrical hohlraums, which was confirmed through the experiments. Further, the DD neutron yield in the experiments would scale to a yield comparable to the highest neutron yields obtained with a DT-filled symcap at similar laser energy and power using the low-foot National Ignition Campaign–style pulse shape.

The third article describes efforts to automate NIF target characterization and defect removal. During the glow-discharge polymer coating process, any small defects that remain on the surface are coated over, and a "dome" is subsequently grown over the top of it. A process has been developed to automate the subsequent dome removal process by combining capsule handling, mapping, and laser polishing all into one physical station. With this system, higher and more precise dome removal yields will be achievable, as well as the ability to engineer purposeful designs into the capsule's surface.

The fourth article describes improvements being made to the x-ray framing cameras, the gated x-ray diagnostic and the hardened gated x-ray diagnostic, used at NIF. Progress has been made in characterizing, modeling, and mitigating the effects of two distinct yet coupled phenomena observed in these cameras: artifacts due to incident radiation before the detector is triggered and variability in gain and inter-strip timing due to electromagnetic coupling. These two phenomena can have detrimental effects on data analysis when quantitative precision is desired.

Laser polishing to remove surface defects on NIF ignition capsules

E.L. Alfonso[1], T. Bunn[2], and L.C. Carlson[1]

[1] General Atomics, San Diego, USA
[2] Lawrence Livermore National Laboratory, USA

I. Introduction

The National Ignition Facility (NIF) ignition capsules are about 200 μm thick glow-discharge polymer (GDP) capsules [1]. Meeting the surface roughness specification is a main requirement for these capsules. This specification consists of several different specifications depending on scale length, which are further divided into "homogeneous" roughness and isolated defects requirements (which can include debris). The homogeneous surface requirements are routinely met, and with high yield. However, the specification currently presenting the greatest challenge, and which reduces yield, is the newly-tightened isolated features specification. The primary offenders are features slightly greater than 0.5 to 1 μm in height, and about 40 to 100 μm in diameter. They are an unintended consequence of micron-scale debris in the vapor-deposition process used to make the capsule [2, 3]. Most of the remaining features (e.g., less than 1 μm) have been eliminated through the development of a tumble-finishing technique at Lawrence Livermore National Laboratory (LLNL) and General Atomics (GA) [4, 5]. However, the tumble-finishing technique is unable to fully remove features in the aforementioned diameter range and height greater than 1 μm, and may increase mid-mode roughness.

We have developed a process to remove or reduce the height of the offending features. This novel technique uses a series of pulses, fine-tuned in time and size, from an ultraviolet laser to ablate the remaining features to levels below the specification, or to where they can be removed using the abovementioned tumble-finishing technique. The result is an improvement in shell surface finish and increase in NIF capsule fabrication yield.

II. Manual laser polishing (single pulses)

Currently, the laser polishing production step for capsules used in ignition experiments on NIF requires that an operator tailor an ablation crater to match each differently sized defect. Nearly 100 capsules were laser-polished in 2013. The idea of using laser pulses to modify the capsule surface is not new [6, 7]. This work focuses on removal of features to smoothen the final capsule surface.

The laser used is a Coherent Avia diode-pumped, solid-state Q-switched laser, operating at 266 nm wavelength. It operates at a maximum of 3 W average power at 30 kHz with a pulse width of ~15 ns. This laser is used specifically for its short pulse width to minimize thermal damage to the surrounding area. It is routinely used for micro-machining and shaping polymer foils and bulk material. The system layout is shown in Figure 1. The beam is directed through a wave plate polarizer/beam-splitting cube to attenuate power output. The beam can be masked to create nearly top-hat ablation craters, or unmasked to ablate Gaussian-shaped pits. For further power reduction, a 98% AR-coated partial reflector was incorporated when necessary. A final focusing lens (f50) is used to

direct the beam onto the sample. The sample is originally aligned with the workstation's viewing camera and moved into position of the laser on Aerotech A3200 precision motion stages. The stages can move the sample in 4 axes (x, y, z, and u) with positional accuracy within ±1 µm.
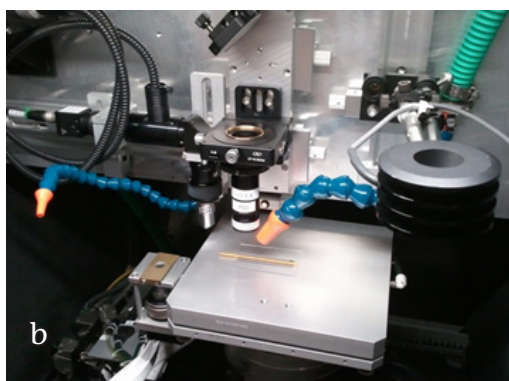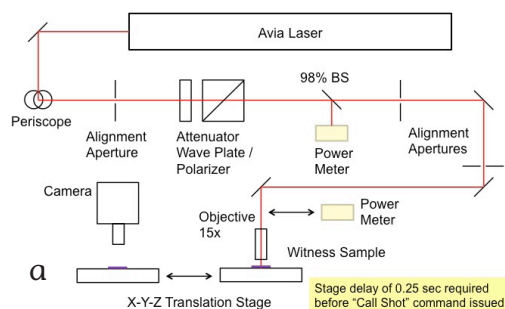

Figure 1: *(a) Schematic layout of the laser beam path. (b) Photo of the precision X, Y, and Z translation stages, gas assist, relay objective lens, camera system, and power meter.*

Before working on the CH ignition capsules, a surrogate CH capsule is used to determine the material removal function at a specific laser power. The beam is masked with a pinhole aperture to create a focused beam size slightly less than the diameter of the defect. The pit ablated by a single pulse is measured on a Wyko optical profiler. With the current laser conditions, the depth is about 200 nm/pulse, and the pit is flat-bottomed. The desired ablation crater would be such that the laser is pulsed the number of times necessary to reduce the offending feature to less than 500 nm tall without ablating more than 100 nm below the surface. If several pulses are needed due to the

height and/or width of the feature, the beam is moved in a circular, overlapping raster pattern to ablate a tapered pit that is the approximate "inverse" of the dome feature.

The entire surface of each ignition capsule is mapped over 4pi using a phase-shifting diffraction interferometer (PSDI) [8]. A list of defects on capsule that qualify for laser polishing due to their size is created from analysis of PSDI data. These are defects that would not meet the final mix mass criteria with tumble finishing alone. Therefore, these defects must be initially reduced in size by laser ablation prior to tumble finishing. The capsule is carefully mounted under an optical microscope onto an adhesive pad so that the offending feature is on top of the capsule. Each defect size and shape is measured again with the Wyko profiler. From comparison to images from the PSDI medallion, we can give an identity to each feature. The capsule is brought into the laser system and the defect is targeted in the viewing camera. The laser is fired with parameters and stage position locations prescribed by the surrogate test to ablate the defect. The defect is measured again and the process is repeated until the defect remainder meets the size requirements for tumble finishing. Camera and confocal microscope images of a simple, single-shot raster pattern are shown in Figure 2.
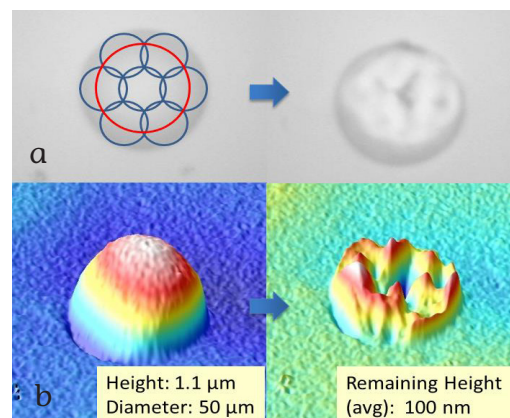

Figure 2: *(a) Camera view of dome before and after simple seven-shot raster pattern (outlined above dome). (b) Confocal microscopy of same dome before and after laser ablation.*

Shown in Figure 3 are profilometer traces of a 900 nm tall feature before and after laser polishing. The height and width of the remaining "wings" of the defect are within the size regime to be tumble finished to negligible mix mass. Guided by the PSDI defect list, the capsule is reoriented under an optical microscope to find the next defect on the hit list. The size characterization and surrogate ablation analysis is repeated and the procedure continues until all defects are below the polishing threshold.
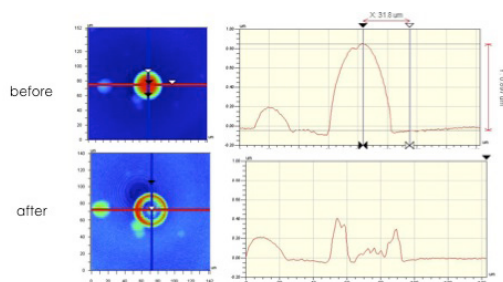

Figure 3: *Wyko profilometer lineout of 900 nm tall defect before and after laser polishing.*

III. Raster patterns based on common defect sizes

Most defects on capsule surfaces are dome-shaped, growing from an initial seed early in the coating process [9]. From established models of defect growth, if the initial seed is 1 μm, final dome size on a nominal 200 μm thick capsule is 1 μm tall and 40 μm wide. Due to the regular growth behavior, there are a few common dome-shaped defect sizes. A more robust approach to ablating various sized dome-shaped defects is to use a small ablation pulse in a finely spaced circular raster pattern. This approach could more easily be tailored to varying defect sizes. Instead of continuously changing the mask aperture to match the defect size and ablating test patterns in surrogates, one could select predetermined pattern recipes using several hundred small laser pulses stitched together.

The laser system was altered by removing the mask aperture and installing a partial reflector

to attenuate most of the laser energy. Operating at 30 kHz, the laser was attenuated to 5 mW average power. We ablated pits in a flat GDP sample at 10 pulses per location, shown in Figure 4. The pits were Gaussian and had an average depth and width of 4.6 nm/pulse and 7.2 μm/pulse, respectively. The average depth of the pits varied by nearly 50%. After the experiment was concluded, the laser's fourth harmonic generation crystal temperature control loop was shown to be malfunctioning. This caused unstable laser power output, which was the most likely cause for the ablation pit variation. When pulses were stacked on a single ablation site, the depth of the pit was linear with the number of pulses. The material removal function for total and average depth per pulse is shown in Figure 5. We used this information to determine the required number of pulses in the center of the circular raster pattern (maximum height).
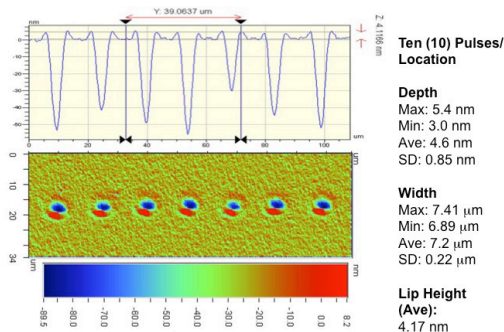

Figure 4: *Ablation pits in GDP surface. Laser 5 mW average power, 17 μJ/pulse*.
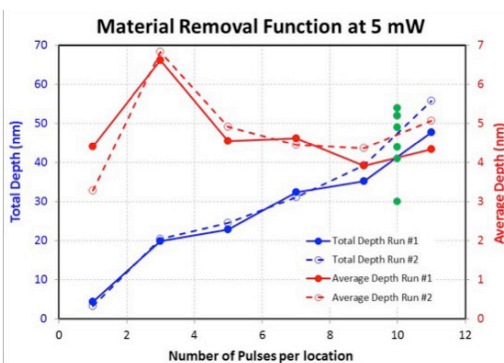

Figure 5: *Total and average depth of ablation pits in GDP.*

To model the dome-shaped defect, the raster pattern was based on concentric rings. We

assumed a constant ablation removal function. Inputs to the program included overlap between pulse diameter along ring circumference, pulse diameter overlap between rings, pattern width, number pulses in center ring, functional form or pulse roll-off (quadratic or linear), and pattern constructed outside-in (fixing width first). A typical raster pattern could contain 1500 individual laser pulses and would take ~2 minutes to complete.

The nomenclature of the raster patterns was based on percentage of overlap in the radial (R) or circumferential (C) direction. Examples of raster patterns with varying amount of overlap are shown in Figure 6. The amount of overlap controlled the pattern depth, and a variety of pit depths could be created, as shown in Figure 7.
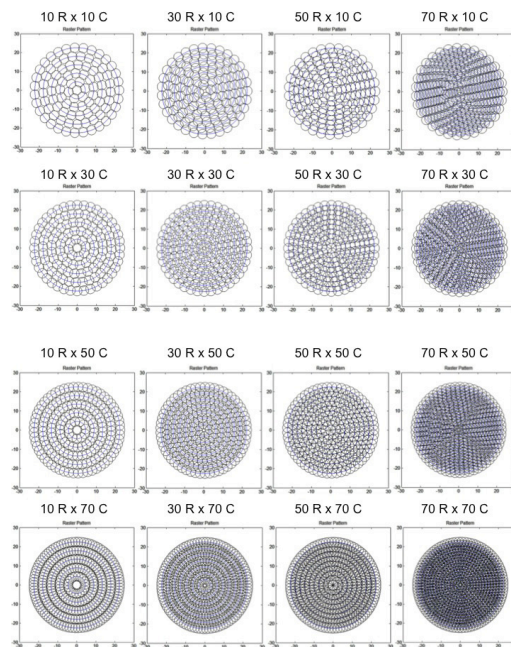

Figure 6: *Sample circular raster patterns for dome-shaped defects. Each circle within a pattern represents an ablation site. The percentage of overlap in the radial (R) and circumferential (C) direction is shown.*
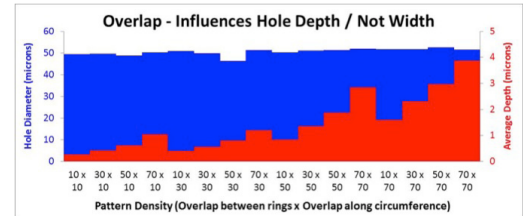
Figure 7: *Average crater depth for the array of raster patterns with varying overlap.*

We used a laser pattern with 50% overlap in the R and C directions to test the repeatability of a single pattern. Profilometer lineouts are shown in Figure 8 for four representative pits. The variation in pulse-to-pulse ablation depth is smoothed out over many hundreds of pulse locations. The pits had a base width of 50 μm and total depth of about 1 μm and showed good repeatability. A library of ablation patterns for the crater shape can be generated with different combinations of R and C overlap for the most common defect sizes. These could be matched to the PSDI defect list to select the appropriate raster pattern for each defect.

Figure 8: *Reproducibility of a raster pattern composed of several hundred pulse locations. Each crater was about 50 μm in diameter and 1 μm deep.*

IV. Automated laser polishing

Current capsules require laser polishing of 1–3 large defects per capsule; the remaining smaller defects (<500 nm tall) 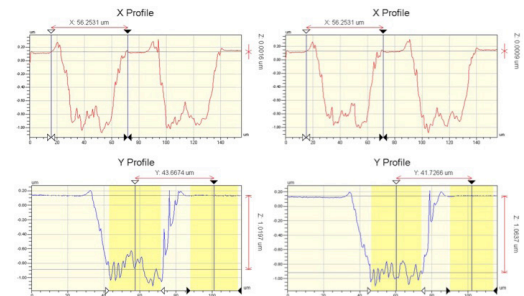are removed by tumble polishing. Future requirements may include eliminating the tumble-finishing step entirely. This would require laser-polishing tens to hundreds of defects per capsule. To meet this requirement, a laser system with in-situ characterization and automated capsule handling is currently under development [10].

An algorithm for defects of varying size and shape is being developed, which rasters together many individual low-energy laser pulses, custom-designed for each unique defect. The defect is not always a round, dome-shaped feature. This algorithm can also be tailored to produce modified capsule surfaces (features and patterns). Finally, this automated system would minimize the operator's input and could polish capsules autonomously.

V. Conclusions

An ultraviolet laser system is successfully used to reduce offending surface feature sizes to a regime where they can be completely removed by tumble finishing. For few features per capsule, it can be operated by individually tailoring the ablation crater to match the defect size. Since many of the feature share a common shape and size, we are developing raster pattern recipes for these common sizes without having to test in surrogate material. Finally, these techniques can be further incorporated into a fully autonomous system with automatic capsule handling, defect finding, laser ablation, and in-situ characterization.

VI. REFERENCES

[1] A. Nobile et al., "Status of the development of ignition capsules in the U.S. effort to achieve thermonuclear ignition on the national ignition facility," *Laser and Particle Beams* **24**, 567–578 (2006).

[2 A. Nikroo et al., "Progress in 2mm Glow Discharge Polymer Mandrel Development for NIF," *Fusion Science and Technology* **45**, 165–170 (2004).

[3] A. Nikroo and D.M. Woodhouse, "Bounce coating induced domes on glow discharge polymer coated shells," *Fusion Science and Technology* **35**, 202 (1999).

[4] D.G. Czechowicz et al., "Investigation to remove domes from plastic shells by polishing," *Fusion Science and Technology* **51**, 600–605 (2007).

[5] T.I. Suratwala et al., "Polishing and local planarization of plastic spherical capsules using tumble finishing," *Applied Surface Science* **261**, 679–689 (2012).

[6] M.D. Shirk et al., "Laser machining for fabrication of hohlraums and capsules," *Fusion Science and Technology* **49**, 479–487 (2006).

[7] R.J. Wallace et al., "*Laser Ablation Machining of ICF Capsules,*" LLNL document (1994).

[8] Y.T. Lee et al., "Increasing the Throughput of Phase-Shifting Diffraction Interferometer for Quantitative Characterization of ICF Ablator Capsule Surfaces," *Fusion Science and Technology* **55**, 405–410 (2009).

[9] S.A. Letts et al., "Ultrasmooth Plasma Polymerized Coatings for Laser Fusion Target," J*ournal of Vacuum Science and Technology* **19**, 739 (1981).

[10] L.C. Carlson et al., "Automation of NIF Target Characterization and Laser Ablation of Domes Using the 4pi System," in production for this issue.

Rugby hohlraums on the National Ignition Facility

P. Amendt[1], J-P. Leidinger[2], J.S. Ross[1], E. Storm[1], D.A. Callahan[1], P. Gauthier[2], D. Hinkel[1], B. Lasinski[1], S. Liberatore[2], P-E. Masson-Laborde[2], D. Meeker[1], P. Michel[1], J, Milovich[1], J. Moody[1], F. Philippe[2], and M. Schneider[1]

[1]Lawrence Livermore National Laboratory, Livermore CA USA 94551
[2]CEA DAM-Ile de France, 91297, Arpajon CEDEX, France

Abstract. Implosions using rugby-shaped gold hohlraums driven by low-adiabat laser pulse shapes have begun on the National Ignition Facility. The rugby hohlraum provides a higher coupling efficiency than a comparably sized cylindrical hohlraum or, alternatively, improved drive symmetry (higher case-to-capsule ratio) and larger laser beam clearances for a larger diameter rugby hohlraum with similar cylinder wall area and laser energy. These implosions used reduced wavelength separation (1.0 Å) between the outer and inner cones to provide a platform free of significant cross-beam energy transfer for simplified hohlraum dynamics. A large-diameter rugby hohlraum shot at low energy (0.75 MJ) to test laser backscatter resulted in a moderately oblate CH capsule implosion, and was followed by a full-energy shot (1.3 MJ) that gave a highly oblate compressed core, according to both time-integrated and time-resolved x-ray images. Post-shot simulations performed at CEA with their radiation hydrodynamics code with a Busquet/Decoster-based non-LTE gold opacity model indicated that repointing the outer cones would improve the implosion symmetry. This was also confirmed at LLNL by adding a phenomenological mix model across the wall/gas fill interface to the standard radiation hydrodynamics code using the high-flux model. A third shot at 1.3 MJ was therefore fielded with a 500 µm pointing change of the outer cones and resulted in a nearly symmetric x-ray self-emission image (P_2/P_0 = 6%) of the compressed core. This demonstration confirmed that the core shape can be controlled in the rugby hohlraum without relying on CBET. The measured DD neutron yield of 1.3×10^{13} would scale to a yield of order 10^{15} for a DT-filled capsule, which is comparable to the highest neutron yields obtained with a DT-filled symcap at similar laser energy and power using the low adiabat National Ignition Campaign-style pulse shape in cylindrical hohlraums. Relatively lower time-dependent symmetry swings were also measured for this third shot, and a significantly lower hot electron fraction was inferred for potentially favorable fuel adiabat control. The outer cone stimulated Brillouin scattering levels increased significantly, but remedial measures such as use of boron dopant in the Au wall are planned.

I. Introduction

Interest in testing rugby-shaped hohlraums on the National Ignition Facility (NIF) is based the results from successful campaigns at the Omega laser facility [1], using both vacuum [2, 3] and gas-filled rugby hohlraums [4]. For gas-filled rugby hohlraums driven by ignition-like, high-contrast laser power histories, the measured peak drive temperatures were nearly 10% higher than in cylinders, the laser–plasma mediated backscatter was low (~1%), capsule implosion symmetry was acceptably round, and the number of DD neutrons established a record ($>10^{10}$) for indirect drive at Omega. For these reasons, a campaign was begun on the NIF to assess the potential advantages of a rugby-shaped hohlraum at ignition scale.

The benefits of a rugby-shaped hohlraum over a conventional cylinder [5] can be

exercised in two ways. First, one can maintain the same radius as a cylinder to take advantage of the approximately 25% reduction in surface area and achieve a nearly 20% improvement in peak drive x-ray flux. On the other hand, one can use a rugby with similar surface area to a cylinder to achieve a similar drive but with improved beam clearances (to the capsule and laser entrance holes) and higher hohlraum case-to-capsule ratio for greater smoothing of hohlraum radiation modes.

The strategy chosen for the initial test of rugby hohlraums on the NIF was to field a 7.0 mm diameter (700) rugby that has ~8% more surface area than the standard 5.75 mm (575) cylinder hohlraum [6]. Figure 9 shows the 700 rugby and the 575 cylinder and the pointing (location) of the 23.5° inner cone. The CCR (R_H/R_{cap}) is 22% larger for the 700 rugby and the clearance for the 23.5° beam over the capsule increases from 0.40 to 0.66 mm, significantly increasing the beam clearance over the capsule. With the significantly larger volume over the capsule, and these hohlraum and capsule/symmetry parameters, the 700 rugby was calculated to have more robust inner beam propagation and thus not require the large wavelength separation between the outer and inner laser beams and the correspondingly large cross-beam energy transfer (CBET) that has been necessary for the 575 cylindrical hohlraums. It was also calculated to have higher overall coupling efficiency of laser energy to x-ray drive and thus, despite the slightly larger area, have a comparable radiation temperature. Early experimental results with a low-foot drive indicate that the rugby hohlraum might eventually serve as a complementary platform for both low-foot, low adiabat [7] (National Ignition Campaign [NIC] style) and "high foot" CH capsules [8, 9] and HDC capsules in gas-filled and near vacuum hohlraums [10].
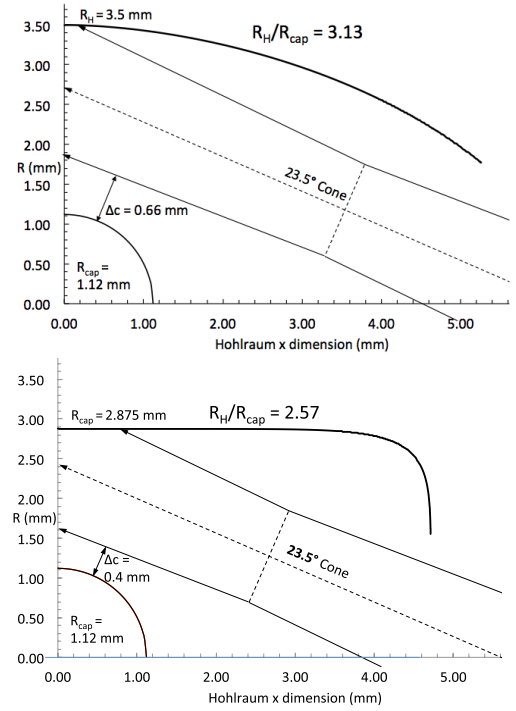

Figure 9: *Comparison of shape, dimensions, and beam path for the inner 23.5° cone for 700 rugby (left) and 575 NIC-type cylinder (right). Also shown are the hohlraum case-to-capsule ratios and clearance of the 23.5° beams above the capsule (Δc). The significantly larger volume over the capsule afforded by the rugby hohlraum is evident.*

II. Experimental Results

The first shot (N130318) was conducted at low energy (0.75 MJ, 300 TW for 1.335 ns) in order to guard against possible high backscatter and risk of damage to the laser optics. The second (N130502) and third (N131011) shots were performed at full energy (1.32 MJ, 370 TW for 2.6 ns). All three shots used a 700 rugby hohlraum with 10.5 mm length, a laser-entrance-hole (LEH) fraction of 50.6%, a hohlraum gas fill density of 1.2 mg/cm³, and a nominal "symcap" CH ablator with buried (1x) silicon-doped layers [11]. The rugby shape was prescribed as an offset circular arc of rotation around the symmetry axis [12]. The shots employed a low-foot, low-adiabat pulse shape, which at full energy is ~20 ns in duration. A mild wavelength separation of 1.0 Å between the outer (44.5°, 50°) and inner

(23.5°, 30°) cones was employed. A pair of static x-ray imagers (SXI) viewing through the two LEHs at 18° and 19° to the hohlraum axis provided time-integrated information on wall motion and laser spots.

II.1. N130318 shot summary

This exploratory first rugby shot used a ^{4}He-filled symcap capsule for imploded core self-emission imaging. Figure 10a shows that the time-resolved equatorial x-ray image in the 3–5 keV region at bang time was oblate with a P_2/P_0 of ~ 40%. The x-ray bang time of the implosion as inferred from the gated x-ray detector (GXD) was ≥22.9 ps. The DANTE-inferred peak temperature was ~250 eV. A gold M-band fraction for energies above 1.8 keV was ~13%, measured by DANTE. The total backscatter energy (~41 kJ) fraction was only 6%, residing almost entirely in stimulated Raman scattering (SRS) from the inner cones and only a small amount (<3 kJ) in stimulated Brillouin scattering (SBS). The SRS from the inner cones relative to the total incident energy was approximately half that seen in the cylindrical NIC-style hohlraums. The degree of hot electron generation as deduced by the FFLEX diagnostic was low, corresponding to hard x-ray production of less than 5 KJ (over the range 20–80 keV) with harder x rays above 170 keV amounting to less than 1 kJ. In summary, the coupling efficiency of laser energy to x-ray drive energy was high (~94%), but with a marginal implosion symmetry.

Pre-shot simulations at Lawrence Livermore National Laboratory (LLNL) and CEA with SRS and SBS backscatter fractions similar to that observed for cylindrical hohlraums had both predicted a prolate imploded core. However, LLNL post-shot simulations using measured backscatter energies still predicted a prolate imploded core, and a bang time approximately 400 ps earlier than measured. Post-shot simulations carried out at the CEA laboratory at DAM-Ile de France (discussed in more detail

below) with an improved wall opacity model and improved hohlraum zoning still had the bang time approximately 400 ps early, but the simulated x-ray images at 100 ps before and after bang time (Figure 10b and c) were oblate with P2/P0 values close to the measured value.

Figure 10: (a) Gated x-ray detector (GXD) image at time of peak emissivity for shot N130318 showing average size (P0) and normalized second Legendre moment distortion (P2/P0) of 17% contour (white line). (b) Post-shot simulations by CEA DAM-Ile de France at 22.4 and (c) 22.6 ns, respectively.

II.2. N130502 shot summary

The next shot was performed at full energy (1.32 MJ, 370 TW for 2.6 ns). Otherwise all other target and laser parameters were the same as for the first, low-energy shot. This nominal full-

energy rugby shot used a ^{3}He-D filled symcap capsule for core self-emission imaging and neutron data generation. Figure 11a shows that the time-resolved core image (3–5 keV) at bang time was even more oblate ($P_2/P_0 \sim$ -66%) than the first rugby experiment. The time of peak x-ray emission of the implosion was 22.25 ns, according to both the GXD and the streaked polar instrument for diagnosing energetic radiation diagnostic, and the DANTE peak temperature was ~280 eV with a gold M-band fraction of ~18%. The total backscattered energy (~90 kJ) was only 7% of the incident laser energy, and as for the first rugby shot, composed almost entirely of SRS from the inner cones and only a small amount (<5 kJ) in SBS. The DD neutron yield was 1.8×10^{11}, and the peak deuterium ion temperature from the neutron time-of-flight diagnostic was 2.1 keV. The degree of hot electron generation as deduced by the FFLEX diagnostic was again low, corresponding to a hard x-ray production less than 30 KJ (over the range 20–80 keV), with harder x rays above 170 keV less than 0.6 kJ. The significantly reduced FFLEX x-ray signal compared with 575 cylindrical hohlraums (~3x) is likely due to the reduced SRS, resulting from the low wavelength separation (1.0 Å) used and the correspondingly reduced CBET from outer to inner beams.

In summary, the coupling efficiency of laser energy to x-ray drive energy was still high (~93%), but the implosion symmetry was even more oblate than for the first rugby shot. This was confirmed by post-shot simulations by CEA DAM-Ile de France (Figure 11b), which showed that for this high-energy shot the Au wall motion near the laser entrance hole was larger than pre-shot simulations done at LLNL. Post-shot simulations carried out at LLNL using a phenomenological mix model [13], as described further below, also showed this enhanced Au motion.
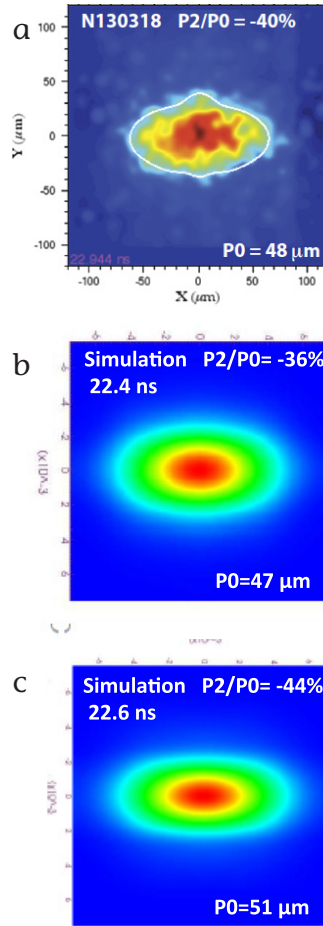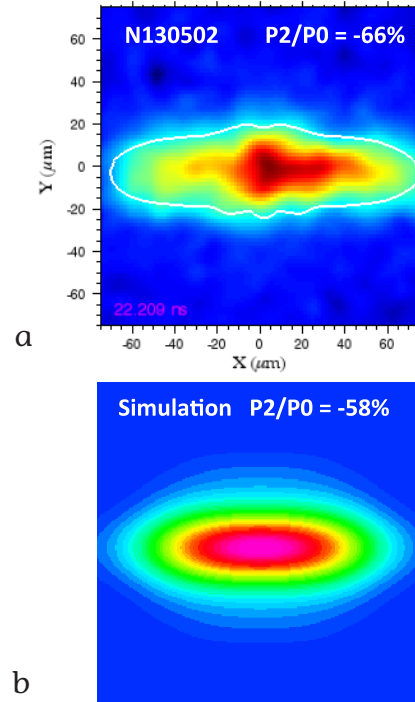

Figure 11: *(a) GXD image at time of peak emissivity for shot N1300502 showing average size (P0) and normalized second Legendre moment distortion (P2/P0) of 17% contour (white line). (b) Post-shot simulations by CEA DAM-Ile de France.*

II.3.   N131011 shot summary

The third shot in the series again used the full laser energy of 1.3 MJ, but with a repointing of the outer cone beams 500 microns along the direction of the hohlraum axis towards the target midplane (suggested by both the CEA and LLNL post-shot simulations of shot N130502) to correct the asymmetry in the core x-ray emission observed on shot N130502. The outer beam pointing (on both the 44.5° and 50° cones) was also modified to split the quad pointing to more uniformly illuminate the hohlraum wall. A small fraction (2.45 at.%) of neon was added to the pure deuterium hohlraum gas fill to study the effect of mid-Z dopant on SRS. The x-ray core self-emission was significantly improved compared to the previous shot, as demonstrated by the nearly round equatorial core ($P_2/P_0 \sim$ 6%) and polar core (*M2/M0*~ 6.5%) images shown in Figure 12.
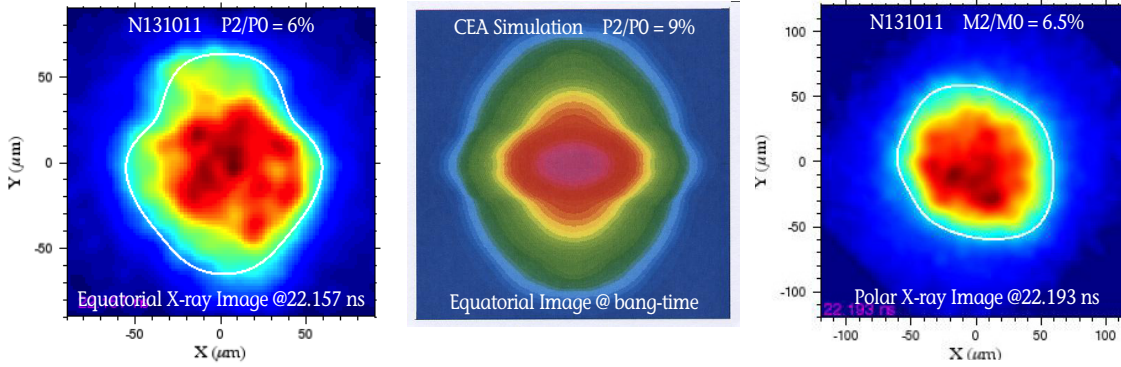
Figure 12: *Gated and simulated x-ray images at time of peak emissivity for shot N131011. (Left) Equatorial image at 22.157 ns. (Middle) CEA post-shot simulation of equatorial image at bang time. (Right) Polar x-ray image at 22.193 ns. The significant improvement in symmetry from shot N130502 is evident.*

The time of peak x-ray emission was 22.2 ns, which is very similar to N130502. The peak temperature measured by DANTE was ~276 eV. The total backscattered energy (~160 kJ) was higher than the previous shot due to an increase in SBS on the 50-degree beams. The SRS was again low (~90 kJ), although a significant reduction in hot electron generation (~4x) was also observed. The FFLEX diagnostic measured less than 5 KJ (over the range 20–80 keV), with hard x rays above 170 keV less than 0.1 kJ. This may be due to the neon in the hohlraum gas fill, which will be further explored and isolated with dedicated experiments. Unexpectedly, the SBS reflectivity in the outer cone (50°) markedly increased to nearly 12%, presumably due to the large-scale outer cone pointing change. The DD neutron yield was comparably high at 1.3×10^{13}, with a peak deuterium ion temperature of 2.6 keV.

In summary, the coupling efficiency of laser energy to the rugby target was modestly high (88%) compared to the conventional 575 cylinders. The high coupling efficiency is mainly due to the reduced inner beam intensity from the low wavelength separation used, and the attendant relatively low values of SRS. As with the previous rugby shots, this higher coupling resulted in a peak temperature comparable to that for 575 cylinders for similar laser energy and peak power, even though the 700 rugby area was slightly (8%) higher. Round x-ray core emission was achieved at 1.0 Å

wavelength separation by changing the outer beam pointing. This demonstration confirmed that the core shape can be controlled in the rugby hohlraum without relying on the use of CBET. We also note that the DD neutron yield would scale to a yield of order 10^{15} for a DT-filled capsule, which is comparable to the highest neutron yields obtained with a DT-filled symcap at similar laser energy and power using the low-foot NIC-style pulse shape.

III. Simulation Results

By far the greatest anomaly observed in the first two rugby shots was the large imploded core asymmetry, particularly for the second rugby shot (N130502). According to mainline 2D radiation hydrodynamics (RH) simulations at LLNL using the "high flux model" (HFM) [14], which is characterized by the generous use of an electron thermal flux limit of 0.15 and a detailed configuration accounting atomic physics non-local-thermodynamic equilibrium (NLTE) model, the imploded cores were close to round or even mildly prolate in shape for the beam pointing used for the first two shots.

As discussed during the analysis of the first two experiments, the leading explanation for the large difference is that the pointing of the outer beams outer lead to a higher pole irradiation due to elevated Au wall motion

near the laser entrance holes (LEHs). Post-shot simulations at CEA DAM-Ile-de France using a Busquet/Decoster-type NLTE model [15,16] that results in a less emissive (or hotter) wall appears to provide the necessary wall motion compared with the LLNL HFM and matched the first two rugby core implosions (Figure 10 and Figure 11). Their pre-shot simulation of N131011 was also very close to the measured shape (Figure 12). The CEA post-shot simulations also show good qualitative agreement with the SXI images for shot N130502 (see Figure 13) and the change in SBS from the outer 50° beams from N130502 to N131011 caused by repointing the outer beams (see Figure 14).
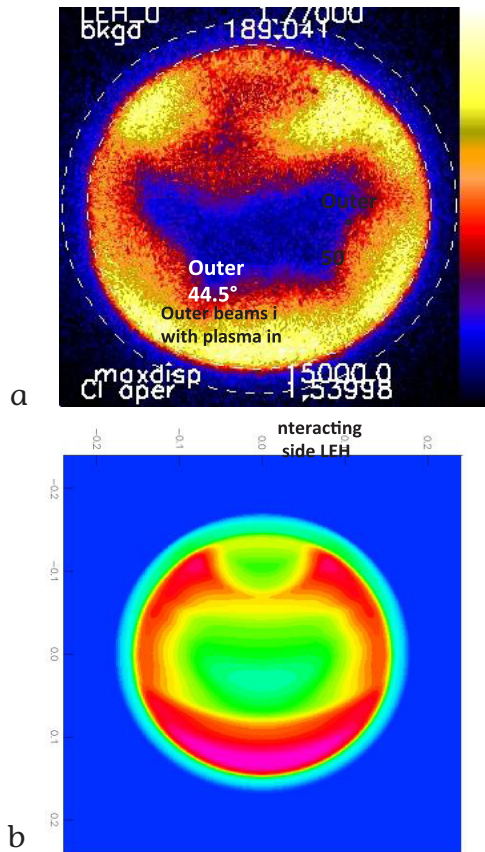

a

b

Figure 13: *(a) Time integrated static x-ray image (SXI) of N130502 and (b) post-shot simulated SXI image from CEA DAM-Ile-de-France demonstrate good qualitative agreement.*
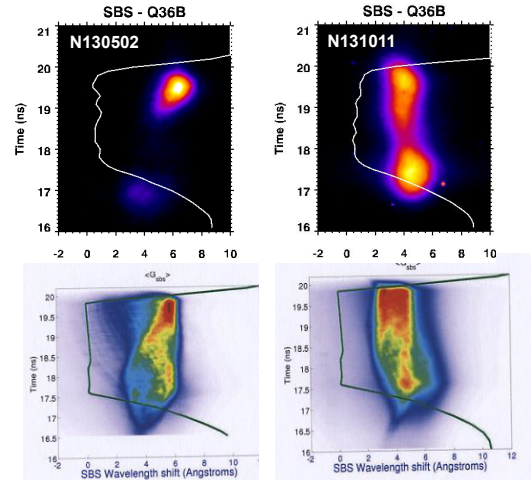

Figure 14: *Measured (left) and post-shot simulated (right) time and spectrally resolved SBS for shot N130502 and N131011 show good qualitative agreement.*

An alternative simulation approach developed at LLNL is to append a phenomenological mix model [13] to the HFM to model hydrodynamic/diffusive mix of Au with the confining helium gas at the wall/hohlraum-fill interface. The simplest and most physically appealing mix model to incorporate in mainline RH simulations is the fall-line mix model [17, 18]. The fall-line model is a prescription for mixing interface material (in this case the wall/hohlraum-fill interface) a prescribed ("penetration") fraction h_p of the distance from the "clean" interface to the fall line, or straight-line trajectory of material ejected away from the interface at the instant of peak interface speed. With a penetration fraction hp of 100%, this phenomenological mix model provides an increased level of wall motion (~200 mm) at the LEH and matches the asymmetry as observed in the experiments. The physical basis for invoking a mix model across the wall/gas interface is the large Atwood number and long episode of deceleration persisting for over 12 ns, providing the necessary conditions for Rayleigh–Taylor instability growth. The candidate seed for potential instability growth may be due to laser speckle since only 1D smoothing by

spectral dispersion is implemented in the experiments. Work continues to refine the relative roles of hydrodynamic/diffusive mix across the wall/gas interface and non-LTE wall physics modeling in interpreting the rugby hohlraum results.

IV. Future directions

The immediate application of rugby hohlraums is to develop a simplified hohlraum platform with minimized CBET effects for high-foot experiments. An immediate performance milestone is to reduce the SBS levels to manageable levels (<5%) by a combination of outer cone repointing and the use of boron dopant in the Au for increased Landau damping. Once the backscatter is satisfactorily controlled, the expectation is that improved time-dependent symmetry behavior will occur along with the added benefit of reduced preheat generation, based on successful results with the low-foot laser drive.

After the symmetry advantages of rugby hohlraums have been validated for the current high-foot capsule/pulse shape, the next step is to explore the use of the rugby geometry for high-foot capsules with different, lower adiabat and adiabat shaping pulse shapes.

We also plan to explore the use of the rugby platform for HDC implosions in both gas-filled and near-vacuum hohlraums.

V. **References**

[1] T. Boehly et al., "Initial performance results of the OMEGA laser system," *Opt. Commun.* **133**, 495 (1997).

[2] F. Philippe et al., "Experimental Demonstration of X-Ray Drive Enhancement with Rugby-Shaped Hohlraums," Phys. Rev. Lett. **104**, 035004 (2010).

[3] H. Robey et al., "High performance capsule implosions on the OMEGA Laser facility with rugby hohlraums," *Phys. Plasmas* **17**, 056313 (2010).

[4] F. Philippe et al., "Demonstrated high performance of gas-filled rugby-shaped hohlraums on Omega," *Phys. Rev. Lett.* **21**, 074504 (2014).

[5] P. Amendt et al., "Assessing the prospects for achieving double-shell ignition on the National Ignition Facility using vacuum hohlraums," *Phys. Plasmas* **14**, 056312 (2007).

[6] J.L. Kline et al., "Hohlraum energetics scaling to 520 TW on the National Ignition Facility," *Phys. Plasmas* **20**, 056314 (2013).

[7] M.J. Edwards et al., "Progress towards ignition on the National Ignition Facility," *Phys. Plasmas* **18**, 050901 (2013).

[8] O. Hurricane et al., "Fuel gain exceeding unity in an inertially confined fusion implosion," *Nature* **506**, 343–348 (2014); DOI 10.1038.

[9] H.-S. Park et al., "High-adiabat, high-foot, inertial confinement fusion implosion experiments on the National Ignition Facility," *Phys. Rev. Lett.* **112**, 055001 (2014).

[10] A.J. MacKinnon et al., "High-density carbon ablator experiments on the National Ignition Facility," *Phys. Plasmas* (submitted) (2014).

[11] G.A. Kyrala et al., "Symmetry tuning for ignition capsules via the symcap technique," *Phys. Plasmas* **18**, 056307 (2011).

[12] P. Amendt et al., "Rugby-like hohlraum experimental designs for demonstrating x-ray drive enhancement," *Phys. Plasmas* **15**, 012702 (2008).

[13] P. Amendt et al., *Phys. Plasmas* (submitted) (2014).

[14] M.D. Rosen et al., "The role of a DCA atomic physics package in explaining the energy balance in ignition scale hohlraums," *High Energy Density Physics* **7**, 180 (2011).

[15] M. Busquet, "Radiation-dependent ionization model for laser-created plasmas," *Physics Fluids* **5**, 4191 (1993)

[16] A. Decoster, "Review of the NLTE emissivities code comparison virtual workshop," *J. Quant. Spectrosc. Radiat. Transfer* **81**, 71–84 (2003)

[17] P. Amendt et al., "Indirect-drive noncryogenic double-shell ignitiontargets for the National Ignition Facility: Design and analysis," *Phys. Plasmas* **9**, 2221 (2002).

[18] P. Amendt et al., "An indirect-drive non-cryogenic double-shell path to 1Ω Nd-laser hybrid inertial fusion–fission energy," *Nucl. Fusion* **50**, 105006 (2010).

Automation of NIF target characterization and laser polishing of domes using the 4pi system

L.C. Carlson,[1] N. Alfonso,[1] H. Huang,[1] A. Nikroo,[1] M.E. Schoff,[1] N.A. Antipa,[2] T. Bunn,[2] M.N. Emerich[2]

[1] General Atomics, P.O. Box 85608, San Diego, CA 92186-5608
[2] Lawrence Livermore National Laboratory, USA 94551

I. Introduction

The National Ignition Campaign (NIC) capsules are specified to be precisely smooth and free of defects. Certain specifications determine acceptable out-of-roundness, number and size of defects, and mixed mass [1]. During the glow-discharge polymer (GDP) coating process on the mandrels, any small defects that remain on the surface are coated over and a "dome" is subsequently grown over the top of it. Typical domes are on the order of 40 µm in diameter and 1 µm in height, and there are perhaps ~2–5 ablation-worthy domes per capsule. More domes appearing on the surface contribute to a higher mixed-mass of the capsule. Current production methods include the capability to laser-polish the domes to an acceptable level of ≤ 300 nm. At this point, the capsules may be polished to remove residual material.

Currently, the sequence for dome removal involves three separate stations: the phase-shifting diffraction interferometer (PSDI) mapping station, an ultra-violet (UV) laser workstation, and a white light interferometer (Wyko). Between the mapping and the dome removal, the orientation and identification of the domes and defects are lost and must be manually found again at a later time.

We have developed a process to automate the dome removal process by combining capsule handling, mapping, and laser polishing all into one physical station. A "4pi" capsule handling system using Aerotech stages permits complete mapping of the capsule, one hemisphere at a time, by a Leica confocal microscope. The 4pi capsule manipulation system, known as the "Capsule Fill Tube Assembly (CFTA) Mapping System" was originally designed and built by Lawrence Livermore National Laboratory (LLNL) [2]. We at General Atomics have modified their design to incorporate the ability to lase the capsule while it is held in any orientation.

With this system, higher and more precise dome removal yields will be achievable, as well as the ability to engineer purposeful designs into the capsule's surface. The final aspect being pursued is dome planarization to eliminate the polishing step altogether (which has been shown to introduce undesirable mid-mode degradation.) The final goal is an automated mapping and laser-polishing system with minimal human involvement.

II. Development

The goal of this endeavor was to duplicate and automate the existing process of laser polishing of domes on GDP capsules. This necessitated a capsule-handling system to manipulate the capsule, a mapping system to find and identify the domes of interest, and a laser ablation system. The footprint of the entire system fits on a 5 x 10-foot floating optical table with most of the hardware mounted in a nearby equipment rack.

Borrowing the CTFA mapping system design from LLNL allowed us to get started on the development fairly quickly. The LLNL mapping
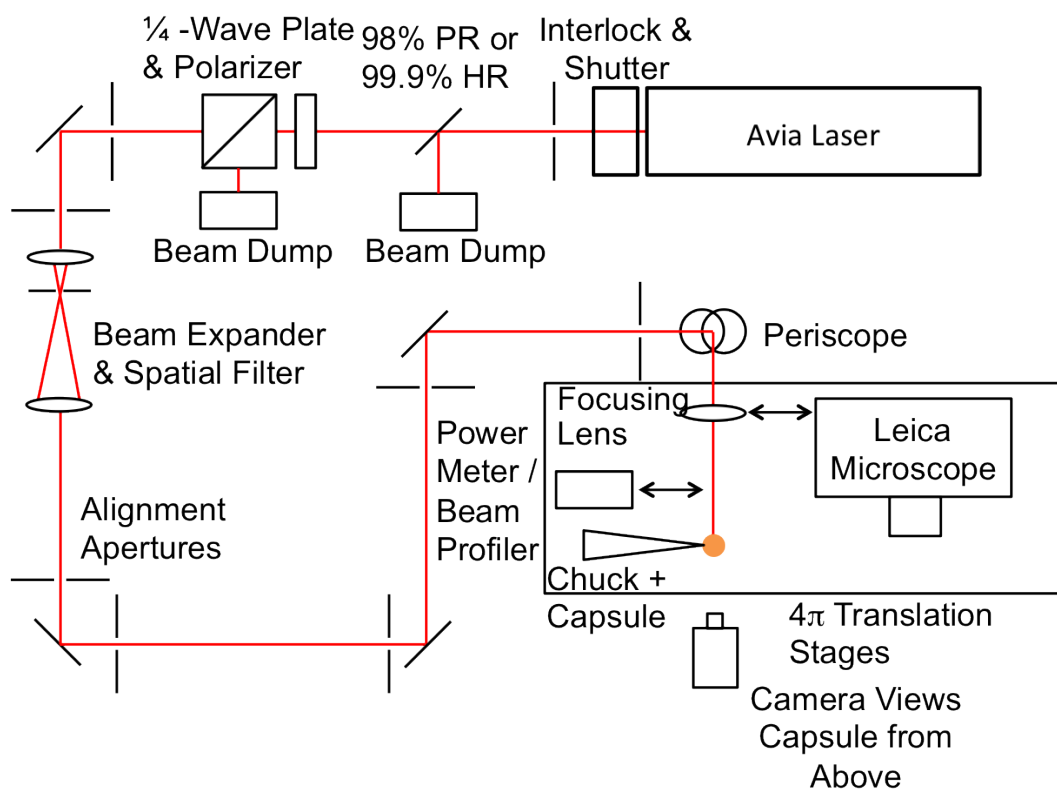
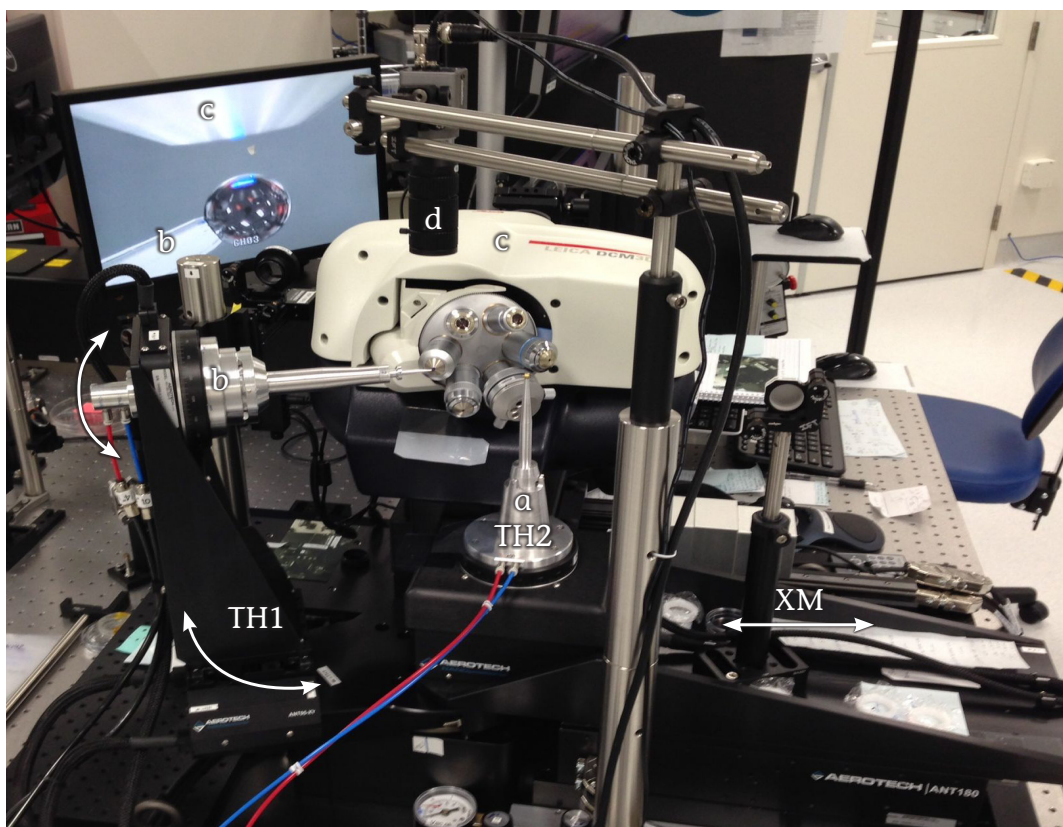**Figure 15:** *Schematic of optics and laser integration with 4pi stage system and Leica microscope.*

Figure 16: *System overview: (a) vertical and (b) horizontal capsule mounting chucks, (c) Leica microscope with phi and theta movements, (d) viewing camera*

system is comprised of seven linear and three rotational Aerotech stages, used in various manners to position the capsule for mapping, position the Leica to maintain focus on the capsule throughout 4pi, and enable CFTA threading. The main modification to the LLNL design is the extension of the Leica's linear slide axis to allow the Leica to move out of the way and the beam delivery optics to line up on the capsule. The translation of this particular stage is repeatable to ± 125 nm and accurate to ± 350 nm, and all Aerotech stages are accurate to the sub-micron range.

The procurement of an identical Leica DCM 3D confocal microscope also permitted analogous mapping of the capsules, as is done by the LLNL final assembly group. This was highly desired on three fronts: 1) to have identical systems to compare measurements between; 2) to utilize Leica acquisition recipes and communication protocols already developed by LLNL; and 3) to employ the unique capability of the Leica confocal microscope to capture "tall" features, such as domes, that are not reliably reported by the PSDI device.

The laser chosen for the purpose of laser machining and polishing is identical to the current laser workstation, a Coherent Avia 266-3 (266 nm at 30 kHz, max 3 W). This laser was chosen for its reliability, beam quality, and proven success of minimal ablation of plastics and dome removal gained from past experience. The addition of a partial/high reflector and wave plate/polarizer to the beam line allows fine control over the energy of the laser pulses, which is necessary for minimal ablation techniques. The transition between the Leica microscope and the final focusing lens is accomplished by a linear translation stage. The ability to view the ablation site in situ is available through a camera viewing the capsule from above (shown) as well as one viewing through the periscope on-axis to the beam (not shown). The ability to scan and capture the height data of the ablation site is provided immediately after by the Leica microscope.

A major effort was undertaken in parallel to the development of this system to explore this region of minimal ablation for finer ablation control [3]. Through this work, the minimal ablation per pulse for the laser system was reduced 4-fold, from ~200 to 50 nm/pulse in CH.

III. Control hardware and software

A concert of controllers coordinates the mapping, data processing, and laser ablation of the 4pi system. The main software controlling the stage motions is written in Aerotech's "Aerobasic" language. Remote control of the Leica microscope is made through Aerobasic using the Leica software development kit over the local area network. LabView is used to accomplish vacuum solenoid switching, using a multi-function data-acquisition card, during the hemi transfer, to email users status reports, and to control the Zaber linear stages for final optic focus. LabView analyzes the raw Leica data when capsule mapping is complete to identify, sort, and visually map defects (more on this later). Aerobasic also controls the shutter and repetition rate of the Avia laser.

IV. Leica 4pi mapping

A standard 4pi mapping procedure is as follows: depending on the capsule size (1 or 2 mm), the user cleans and installs the appropriate set of horizontal and vertical chucks. The user then adjusts the vacuum and mounts a capsule on the end of the horizontal vacuum chuck (no CFTA attached yet). The chuck tips, which touch the surface of the capsule, are sized appropriately for the capsule diameter and diamond turned so only a smooth, normal surface touches the capsule. The user then runs the appropriate Aerobasic program to initialize and home the stages and move the capsule into the

mapping position. The Leica microscope then travels forward and automatically focuses on the surface. Some fine manual adjustment is done to center the capsule in the Leica's field of view. After initialization, a calibration routine might be run to ensure that the capsule's surface remains in the Leica's field of view and focus throughout phi (rotational) and theta (transverse) motions. This is necessary to account for mounting and misalignment errors as well as chuck runout. In practice, after the calibration, the stages move in unison as directed by the synchronization cam tables to ensure the capsule's surface remains steady.

The Aerobasic mapping program is then run, and the user selects from a variety of menus to identify the capsule type, coating type, size, name, and ID, and to specify what is to be done at what magnification: map one hemisphere only, conduct hemi flip only, or map the entire capsule (composed of two hemi maps with hemi transfer). A variety of different Leica parameter "recipes" are called by Aerobasic depending on the characteristics of the capsule. Parameters included are the objective type, light source, light intensity, scan range, topology technique, and surface flattening. Once final parameters are confirmed, the system begins the mapping, and the user is free to return in 45 minutes (1 hemi, 60 medallions) or 1.5 hours (full 20x 4pi mapping, 120 medallions). Other less frequently used recipes include 50x mapping

in 4.5 hours and 100x mapping in 16 hours. Depending on the objective selected, the mapping program divides up the hemi into the number of medallions needed for full coverage, including a 10–15% overlap between subsequent medallions, which is necessary for stitching later. The phi and theta axes then increment automatically so the Leica can acquire the necessary medallions one after another.

For a mapping-only sequence, the system will proceed to the hemi flip after completing the mapping on Hemi 1. The transfer is necessary because the capsule handling is capable of mapping slightly more than 2pi at a time. The transfer, incorporating the vertical chuck and a series of vacuum solenoids, routinely demonstrates 2–5° in hemisphere alignment and takes ~2 minutes.

V. LabView Leica data processing

For laser ablation of domes, the system stops after mapping Hemi 1 to process and filter the data, then to reimage and ablate the domes on that hemi. Once the raw Leica data is acquired, LabView begins processing the ~60 medallions. The algorithm sequence processes the medallions by removing the capsule's curvature and compiling an average background image from which all the medallions are subtracted. This removes general background noise and skewing that might be globally associated
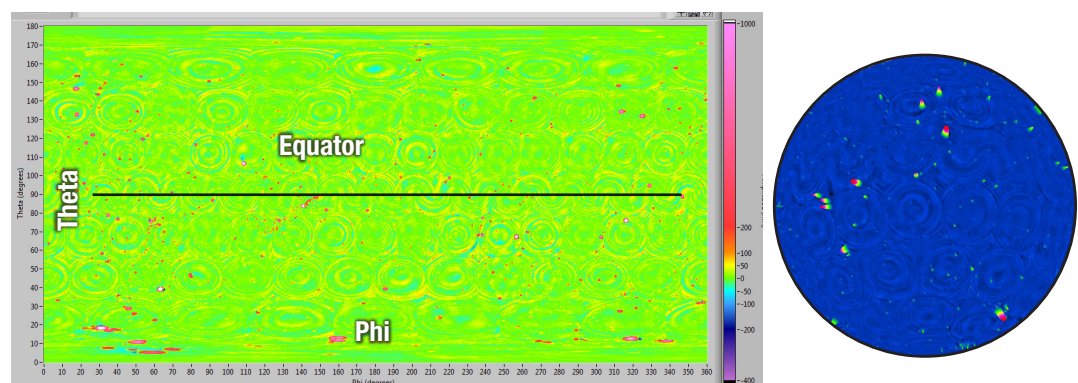

Figure 17: *(Left) 2D mapping of entire capsule. (Right) 3D mapping overlaid on a sphere showing defect heights amplified by 100x.*

with every medallion. The software then runs each medallion through an image analysis algorithm that flags domes or defects above and below a certain height or volume threshold. These are compiled and sorted in a "hit list" that will be used later to reimage and ablate the top 25 domes of interest. Lastly, the software stitches the individual medallions together and creates both a 2D surface and 3D height map of the capsule for keen visualization of the defects.

VI. Comparison to other instruments

In order to validate the Leica mapping technique, we compared PSDI maps and atomic force microscopy patch scans on the same capsule/patch. One cautionary note: the different objectives the Leica has in its turret have different abilities and are used for different purposes. For 2 mm capsules, the 20x objective has been found to be a good tradeoff between medallion coverage per scan (time to map capsule), accuracy of height data, and standoff distance. Drawbacks include small ~50–100 nm rings from vibration/transparency of the capsules, a "potato chip effect" due to possible misalignment of internal Leica components, and a "shadow effect" for domes near the edge of the medallion. Other objectives have advantages and drawbacks in different areas, so a compromise must be reached.

One-to-one comparisons of capsules mapped on the PSDI and Leica show very good correspondence between the two instruments [4]. The quantifiable domes that the PSDI reported in its hit list were similarly reported by the Leica. Deep trenches, fibers on the surface, or other high-aspect-ratio features are not accurately reported by the PSDI but well captured by the Leica. However, the PSDI prevails over the Leica map in smoother background roughness [5]. Overall, the Leica was shown to accurately report the domes of interest, especially when remapped at a higher magnification than the initial 20x scan.

VII. Dome removal by laser ablation

The main purpose of the 4pi system is to remove the domes from GDP-coated capsules using laser ablation. The dome-removal scenario is as follows: map Hemi 1 coarsely at 20x, process the Leica images to compile the hit list, re-image the features of interest at 100x using that hit list, laser ablate those features on that hemi, and then perform the hemi flip and repeat for Hemi 2.

The high-magnification reimaging at 100x is required to better refine the domes of interest for laser ablation. The 20x low mag scan works quickly and coarsely to capture domes and defects above the height threshold, which is nominally 100 nm due to the background noise and residual "rings" seen from flattening the medallions. However, the volume calculation of the domes might be off by two times the actual amount. This is especially true for domes that are captured near the edge of the medallions, which have a "shadow" effect due to the large amount of curvature seen with the 20x objective. The low-mag hit list provides the 4pi system with a set of phi and theta coordinates to reimage the domes at 100x, which takes less than one minute per dome. At this point, the user can then override and conduct a manual circular rastering routine, as is done on the current laser ablation station, or the system can apply a customized raster pattern based on that specific dome's size characteristics. Not all domes are nicely rounded and stand alone; some are clustered together and of unusual height differences. The automated ablation routine takes the 100x image and bins the pixels depending on the a) size of the Gaussian laser beam, b) laser-material removal function, and c) height threshold, or amount of material to leave. The two-dimensional "packing" of the laser pulses was initially accomplished by simple square packing, but more recently hexagonal packing was employed to give a tighter and more uniform final result. The algorithm then creates a raster pattern file containing theta, phi, and the number of
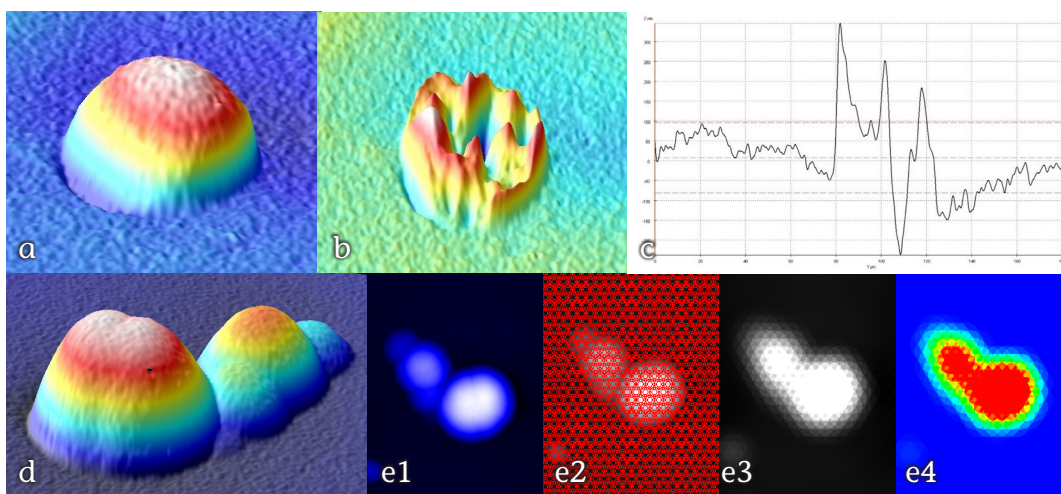
Figure 18: *Laser-polishing example: NOTE vertical scale is ~50x lateral scale. (a) Dome reimaged at 100x giving 1.1 µm height and 50 µm diameter. (b) Residual material after simple laser-ablation pattern. (c) 100 nm average height of lineout of residual material. (d) Irregular cluster of domes requiring custom laser ablation pattern. (e1) Raw 100x image read by LabView. (e2) Overlay of hexagonal-packed ablation pattern optimized for beam diameter. (e3) 100 nm threshold applied. (e4) Shot mapping overlaid on dome with color representing number of pulses per location.*

shots to apply. The 4pi system then travels to those locations and applies the correct number of pulses, assuming the laser is aligned to a known location. This is accomplished with an alignment shot each day/session to ensure the laser, Leica, and capsule are all in alignment.

Some parameters of the laser system normally used for minimal laser ablation techniques are: Gaussian beam profile, f/10 final focusing lens, 30 µm or 15 µm beam diameter (changed by a beam expander before the focusing lens), ~few µJ/pulse, a material removal function (MRF) of ~50–100 nm/pulse, rastering time per dome of ~1–10 min depending on the technique used. Typical domes "worth" removing are on the order of 0.8–1.5 µm tall and 30–60 µm wide. The desired dome height left remaining after laser ablation is < 350 nm but > 50 nm. At this point, the capsules still go into polishing media to remove high-aspect-ratio features; however, this seems to contribute to mid-mode degradation. Once laser polishing of domes has matured, the domes could be planarized right down to the capsule surface so no polishing would be needed.

The initial effort on the 4pi system endeavored to replicate the current method of laser ablation of domes using a manual, simple rastering method. The mapping sequence would identify the domes, and the user would decide on the manual rastering method based on experience. After laser ablation was completed, the capsules would go into polishing for either 4 or 8 days, depending on a polishing algorithm that predicts the final mixed mass based on prior experience of post-polishing metrology of the capsules. The result of this effort over 14 capsules and 29 domes was encouraging. The system performed well compared with the current method of laser ablation of domes conducted. The mixed mass was compared before and after, as is standard procedure, based on PSDI scans and found to be on par. One noteworthy item learned is that it is more detrimental to ablate too deep than not deep enough, since tall, ragged peaks can be removed by polishing, but divots cannot be smoothed. Some of the capsules in this test batch were production quality and continued on through the CH process flow.

Full implementation of the automated dome removal will benefit the CH process by allowing the first PSDI scan to be skipped, since the shell can be mapped and ablated on the Leica 4pi system. A decision tree will

need implementation to autonomously flag domes meeting a certain criteria for laser polishing. The Leica image processing and its interaction with the Aerobasic programs must be streamlined with this decision tree to decide when to ablate and when not to. Lastly, the laser beam alignment and autonomous rastering algorithms over multiple domes on multiple capsules must be fully tested and trusted.

VIII. Conclusions

The 4pi laser ablation system was developed to automate dome removal on GDP capsules. The 4pi system incorporates three main objectives: capsule handling, mapping, and laser polishing of domes. The system has demonstrated reliable and precise capsule handling including hemi transfer, numerous 4pi mappings of capsules, and accurate laser polishing of domes using minimal ablation techniques on numerous production-quality capsules. The sequence and methodology of mapping to laser ablation has been tested with success. The raster algorithms to customize the shots for each unique dome have been employed. The implementation of a decision tree to map and ablate as required is currently in the works.

IX. References

[1] S.W. Haan et al., "Rev3 update of requirements for NIF ignition targets," *Fusion Sci. Technol.* **55**, 227 (2009).

[2] J. Horner et al., "CFTA Mapping System," Final Design Review, internal document.

[3] N.A. Alfonso et al., "Minimal Ablation Techniques" (in print).

[4] H. Huang et al., "Leica 20x Batch Processing and Defect Quantification," internal document.

[5] A.Q.L. Nguyen et al., "Characterization of Isolated Defects for NIF Targets Using PSDI with an Analysis of Shell Flipping Capability," *Fusion Sci. Technol.* **55***, 399* (2009).

[6] R.J. Wallace et al., *ICF Quarterly Report* **4**(3), 79, UCRL-LR-105821-94-3 (1994).

Advances in x-ray framing cameras at NIF to improve quantitative precision in x-ray imaging

L.R. Benedetti, J.P. Holder, M. Perkins*, C.G. Brown, C.S. Anderson, F. Allen, R.B. Petre, D. Hargrove, S.M. Glenn, N. Simanovskaia **, D.K. Bradley, P. Bell

Lawrence Livermore National Laboratory, Livermore, CA, USA, 94550
*now at Varian, Las Vegas, NV, USA.
**now at KLA-Tencor, Milpitas, CA, USA.

Abstract: We describe an experimental method of determining the gate profile in an x-ray framing camera for several important functional parameters: relative gain (between strips), relative gain droop (within each strip), gate propagation velocity, gate width, and actual interstrip timing. Several of these parameters cannot be measured accurately by any other technique.

This method is then used to document crosstalk-induced gain variations and artifacts created by radiation that arrives before the framing camera is triggered. Electromagnetic crosstalk can cause relative gains to vary by several times as interstrip timing is varied. This imposes a stringent requirement for gain calibration. Radiation that arrives before a framing camera is triggered can cause an artifact that manifests as a high-intensity, spatially varying background signal. We have developed a simple device that can be added to the framing camera head to prevent these artifacts.

I. Introduction

X-ray framing cameras are imaging diagnostics that couple a narrow, high-voltage pulse to a leaded-glass microchannel plate that acts as a very high gain amplifier [1–3]. This pairing allows the collection of high-quality x-ray signals with an integration time as fast as 35 ps. Combined with pinhole optics, framing cameras can be used to collect multiple images at different times, effectively creating a high-speed x-ray movie. The x-ray framing cameras at the National Ignition Facility (NIF), GXD (gated X-ray diagnostic) [4, 5] and HGXD (hardened gated x-ray diagnostic) [6], are used to make increasingly precise measurements, especially of the size and symmetry of inertially confined fusion (ICF) implosions [7]. These measurements are made possible by recent advances in the development and operation of x-ray framing cameras that have been achieved at NIF.

In this article, we describe two distinct yet coupled phenomena that have been observed in GXDs: 1) artifacts due to incident radiation before the detector is triggered and 2) variability in gain and inter-strip timing due to electromagnetic coupling. These two phenomena can have detrimental effects on data analysis when quantitative precision is desired. Moreover, understanding the processes that produce these unexpected behaviors requires a sophisticated understanding of the time dependence of the electromagnetic field, not just within the amplifying mechanism, but throughout the entire camera.

We further describe efforts at NIF to characterize, understand, and mitigate the effects of these phenomena. The artifact produced by advanced radiation has been successfully mitigated by the addition of a high-voltage electrode ~1 cm above the surface of the microchannel plate (MCP) that forms the camera's active area. This electrode,

dubbed ERASER (early radiation artifact suppression electrode rig), has minimal effect on the framing camera operation or gain because its high-voltage surface is open above the active area of the framing camera, which successfully eliminates artifacts by attracting any electrons created by x rays that arrive before the camera is triggered.

In contrast, engineering solutions to crosstalk-induced gain and timing variations cannot be solved on a short timescale, as they require wholesale redesign of framing camera input and output circuit boards. While we pursue that strategy as a parallel research effort, we have implemented an operational mitigation strategy. Specifically, when precision is required in analysis, we require that a flat-field measurement be made under the exact same operating conditions (timing and bias voltage) in order to accurately characterize the gain and timing of the camera. In addition, we strongly recommend avoiding operational configurations (timing and bias) that are particularly susceptible to crosstalk-induced gain variation.

II. The amplification mechanism of the x-ray framing camera

Brief description of x-ray framing cameras

Schematic images of the x-ray framing cameras in operation at NIF are shown in Figure 19. X-rays incident on microstrips create electrons, which are then amplified

in the MCP when negative voltage is applied to accelerate the electrons through small channels (pores). Amplified electrons emerge from the channels and are accelerated to a phosphor to produce optical images that can be recorded on CCD or film.

The amplifying voltage is applied as a pulse in order to achieve short integration times. The shape of the voltage pulse and the thickness of the MCP combine to produce a period of high gain ("gate") that is temporally shorter than the initial voltage pulse. For example, cameras at NIF create a ~100 ps gate from a 200 ps voltage pulse and a ~250 ps gate from a 600 ps voltage pulse.

The voltage in the pulse determines gain. However, gain is modulated not by changing the peak voltage in the pulse, but by holding the MCP at a DC bias voltage that is combined with the transiting pulse to produce a total voltage on the MCP. The GXDs at NIF have sufficient primary voltage pulsers to use reverse bias voltage to decrease the total gain (in this usage, "reverse" bias means opposite in sign to the pulsed voltage). This allows for extinction of any non-Gaussian tail of the transiting voltage pulse and functions to keep the gating time of the camera narrow. In contrast, previous designs of x-ray framing cameras have occasionally used forward bias to increase the voltage on the transiting pulse in order to achieve sufficient gain. This method is then susceptible to increased gating time when higher forward bias is used. In contrast, higher-bias (lower gain) settings on reverse-biased framing cameras act to further narrow the gate [3].
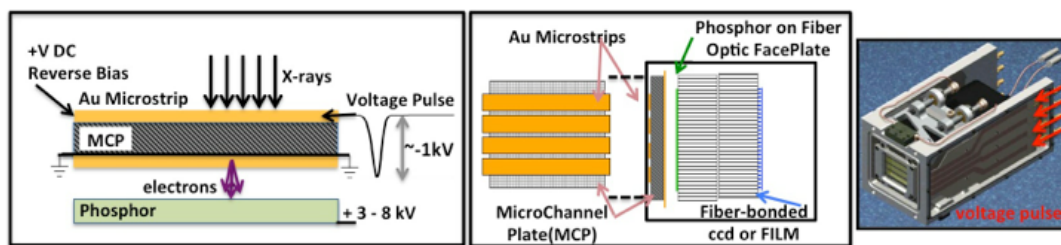

Figure 19: *Schematic of the framing camera [SPIE]. (Left) Side view of the active area and amplification mechanism. (Middle) Top view indicating microstrip geometry and side view showing data collection to CCD or film. (Right) Computer-aided design view of a framing camera head showing input circuit board.*

Because the voltage pulse takes time to travel across the MCP, images that are collected and amplified at different locations reflect the image source at different times. With voltage speeds ~0.5c, a 35 mm–long microstrip records ~200 ps. Framing cameras at NIF are built with either two or four microstrips that are each triggered by independent voltage pulses. In this way the total camera record length of 400 or 800 ps may be recorded continuously or separated by intervals of up to several nanoseconds. The voltage pulses are formed by electronics that are separated from the MCP by nearly 1 m and travel along adjacent paths for relatively long distances before they are used for amplification at the MCP, which may allow independently generated pulses to interact (crosstalk).

At the ~1 kV voltages used in x-ray framing cameras, the MCP is a strong amplifier, and gain is proportional to a high power of voltage (G ~V^{9-12}). As a result, the small reduction in total voltage that occurs due to impedance losses from the entrance to the exit of each microstrip results in significant "gain droop" along the microstrip. Typically, ~5% voltage loss over a 35 mm–long strip results in around 3x gain reduction. This non-uniformity of gain provides a strong motivation to characterize each framing camera carefully.

Precision measurement of the gate profile

Sophisticated methods are required to calibrate the x-ray framing camera when the voltage is pulsed. A well-characterized, high-intensity radiation source that can uniformly illuminate the 35 by 35 mm active area of the MCP is required to mimic the high x-ray emission intensities of a NIF implosion for which the framing cameras have been designed.

The gate profile measurement technique is used to characterize several aspects of framing camera functionality. In this technique, a short-pulse UV laser is used to fully illuminate the active area (MCP) of the framing camera at the same time the camera

is triggered. Because the laser pulse (<1 ps) is much shorter than the camera integration time, a single image gives a snapshot of the location-dependent gain at the time the laser arrived at the MCP surface.

The relative delay between the camera trigger and the laser arrival is recorded by passive electrical monitors on the framing camera and by the arrival of a separately timed leg of the laser to a photon counting detector (with traces recorded on an oscilloscope). Additionally, the energy in each laser pulse is recorded, and image data is normalized by this value to account for variability in the laser.

While a single image yields only limited information about camera operation, two images collected with the laser arriving at the MCP surface at different times relative to the camera trigger can be analyzed (although crudely) to estimate the velocity of the voltage pulse and the relative gain (droop). We take this idea further by collecting a suite of many images over a wide and well-sampled range of time to determine the gain performance everywhere on the camera.

The method is illustrated schematically in Figure 20. In the left image, the front-most rectangle represents a single image of a laser pulse that arrived at the MCP when the voltage pulse was peaked at the right side of the strip (following the convention of NIF framing cameras, the voltage pulse is travelling from right to left). The "stack" of rectangles represents a series of images taken with the framing camera triggered progressively earlier so the laser pulse arrives when the voltage pulse is further along the microstrip.

We start with a data set that is collected as many images, each of which records location-dependent gain at a single time (measured as delay between the camera trigger and the laser arrival). We then reorient that data to reflect time-dependent gain at a single location (Figure 20). Fitting this time-dependent gain to a Gaussian functional form, we determine the arrival time of the center of the gain pulse
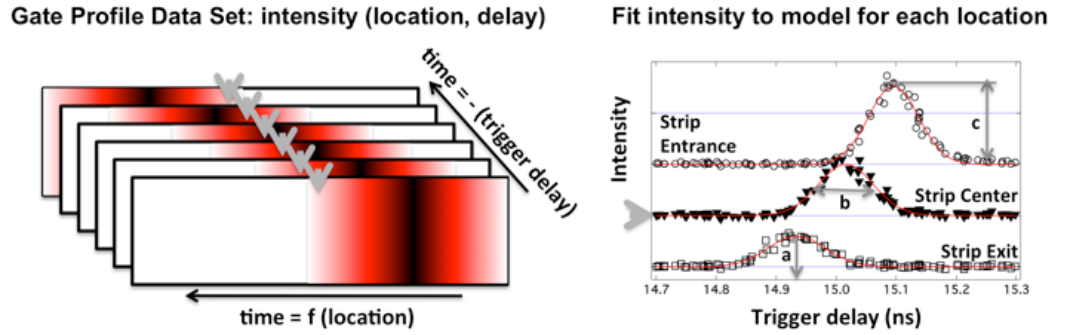
Gate Profile Data Set: intensity (location, delay)

Fit intensity to model for each location

Figure 20: *Gate profile analysis method. (Left) The data set consists of several images triggered at different times relative to the laser. (Right) The normalized intensity at each location (three are shown) is plotted versus trigger delay to determine location-dependent (a) arrival time of peak gain, (b) gate width, and (c) relative gain.*
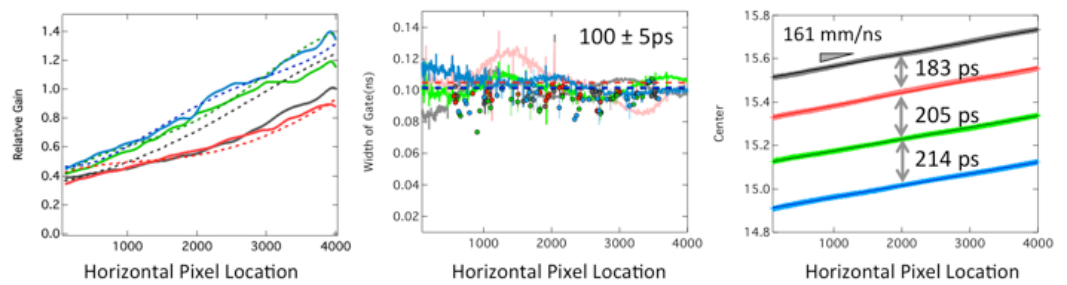

Figure 21: *Gate profile analysis results for a four-strip framing camera operated with 200 ps requested delay between each strip. Results for each strip are plotted with a different color: Strip 1, black; Strip 2, red; Strip 3, green, and Strip 4, blue. Relative gains determined by the gate profile method are compared with flat-field shots on NIF (dashed lines, left).*

(a), the width (full width at half maximum) of the gain pulse (b), and the amplitude of the gain pulse (c). We then repeat the analysis at each location.

Total gain at each location (Figure 21, left, solid curves) may then also be estimated as the area under the Gaussian. Note that we can identify both gain variations between strips—in this case strips 3 and 4 have 20–30% higher gain than strips 1 and 2—and relative gain droop from strip entrance to exit.

The arrival time of the gate at each MCP location (Figure 21, right) also indicates the velocity of propagation of the gate pulse across the MCP; speed is the inverse slope of the arrival time curve. In addition, the offset between arrival time curves indicates the actual time between voltage gain arrival on each strip, which may be slightly different from the request. In the case shown, for example, the time between strips 1 and 2 is 183 ps, though 200 ps was requested.

Gate-width or integration time (Figure 21, center) is not significantly changed across each microstrip, even though total voltage (and resultant gain) is decreasing. However, as bias voltage is increased and total voltage (gain) is decreased, gate width also decreases, consistent with simulations [3, 8]. Once pulse velocity is known, the width of a pulse on a single image can be interpreted as a temporal gating time as well. Inferred gate times for individual images are also plotted as circles on Figure 21, center. These times are in very good agreement with gate widths determined using the entire suite of images at each location.

Uncertainties in the gate-profile measurements are dominated by the number of images collected and by their temporal distribution. Systematic errors are produced when there are small temporal regions that are under-sampled, resulting in an oscillation with fitted Gaussian parameters. This oscillation is clearest in the
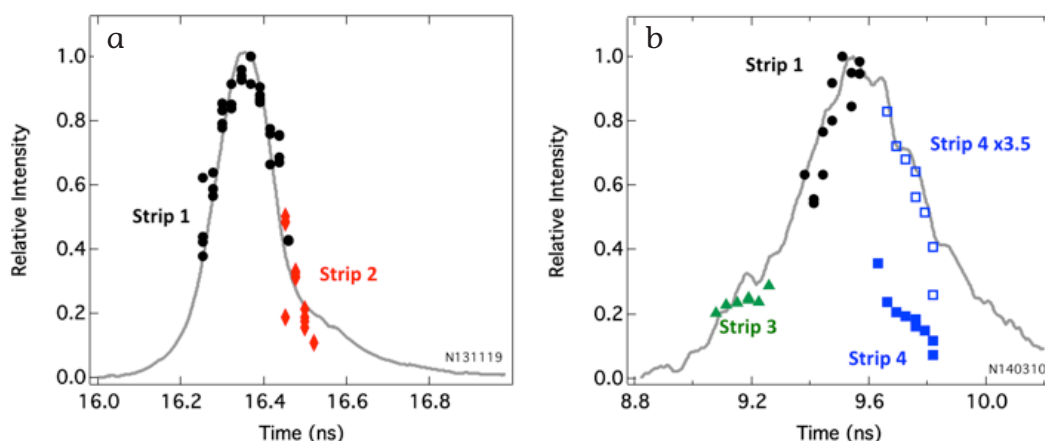
Figure 22: *Relative self-emission vs time in two inertial confinement fusion implosions. Self-emission as measured by the integrated intensity in each image [7] is denoted as markers of different colors or symbols for each different microstrip. For comparison, the integrated self-emission determined by the SPIDER streak camera [11] is shown in the solid curve. In figure a, the image was corrected using flat-field data collected under similar operating conditions, and the inferred self emission from the framing camera is in agreement with SPIDER. In b, an unusual timing and bias voltage configuration was used, and because no flat-field data was available at the correct configuration, the closest configuration was used. Image data was collected with the four independent strips timed at 725, 0, 400, and 1075 ps, respectively, and with bias voltage set to {50, 100, 100, 50} V while the most relevant flat-field had the microstrips timed at {525, 0, 250, 775} ps and the gain set to {50, 50, 50, 100} V bias. As a result, the framing camera data, especially data from Strip 4, does not give a good estimate of x-ray emission.*

fitted values of gate width (Figure 21, center) but is also evident in location-dependent gain and pulse arrival. As the number of images is increased, the oscillation decreases. Systematic or random error in the laser-energy measurement can also have a significant effect on the accuracy of the measurement. For example, we have determined that the entire gate profile measurement must be made with identical neutral filtration between the laser and the MCP. Even when image intensities were normalized with the calibrated optical densities of filters, the presence of differently filtered images led to systematic outliers. Nonetheless, with careful calibration of the laser signal between measurements at different operating conditions, gain variation with bias voltage and interstrip timing can be measured.

The relative gains and droops determined by this technique can also be measured directly with a dedicated flat-field experiment at NIF. In the NIF flat-field experiment, the MCP is uniformly illuminated by Au plasma emission generated by a few dozen beams

of the NIF laser irradiating a gold-coated plastic sphere with a temporally flat pulse [9]. Temporal variation in x-ray emission is measured with a single x-ray diode from the DANTE spectrometer [10] or an x-ray streak camera (SPIDER) [11] and accounted for when determining relative gain.

This method of determining location-dependent gain is direct but very resource-intensive. Relative intensities at different locations on the framing camera image are not well determined unless the flat-fielding data is collected at the same interstrip timing and bias voltage (see Figure 22), requiring a dedicated NIF shot to flat-field each operating condition (timing and bias voltage). For this reason, the development of engineering solutions to reduce gain droop and inhibit timing-related gain variation is an active area of research, both at LLNL and at other facilities [12].

When gate-profile measurements are made at identical operating conditions (timing and bias voltage), the relative gains

and droops determined by gate-profile analysis are in good agreement with those measured in a flat-field shot at NIF (dashed curves on Figure 21, left). Moreover, while the relative gains and droops determined by this technique can also be measured with a flat-field shot, the additional information provided by this analysis—gate propagation velocity, gate width, and actual interstrip timing—cannot currently be measured with accuracy by any other technique.

Using gate profiles to understand and characterize electromagnetic crosstalk

Indeed, this calibration technique was used to identify and characterize gain variations due to electromagnetic crosstalk [13]. Because the microstrips in a framing camera travel close together, their electromagnetic fields are not independent. When a voltage pulse travels through one strip, the other strips act as antennae and receive an induced voltage that is proportional to the temporal derivative of the pulsed signal, increasing with parallel distance traveled. Although the magnitude of the crosstalk signal is substantially smaller than the original signal, the 10–50 V induced signal can cause a significant gain variation (more than a factor of two) if it arrives at the same time as the direct voltage pulse. Moreover, if the induced voltage arrives slightly before or after the pulse, it can also change the effective arrival time of the gain by ~10 ps.

As interstrip timing is varied, the timing of any crosstalk-induced voltage relative to the pulsed voltage (and thus its effect on gain) also changes. This is principally observed as an interstrip timing-dependent gain. Because the width of the voltage pulse that produces gain is ~200 ps (as with all interstrip timings that exceed 200 ps), any voltage induced on one microstrip from its neighbors will not combine with the main pulse to enhance gain. However, when interstrip timings are smaller than ~300 ps, we observe that relative gains vary with interstrip timing.

The gate profile technique is especially useful in documenting crosstalk-induced gain variation because the method also provides an independent measurement of actual interstrip timing along with each measurement of relative gain. For example, we have found that one framing camera (HGXD2) has a greater gain enhancement in Strip 4 at the "standard" 200 ps interstrip timing than other similar cameras. The gate profile indicates, however, that the actual interstrip timing between the third and fourth strips is only 160 ps when 200 ps is requested. At this shorter interstrip timing, the voltage induced from Strip 3 onto Strip 4 combines resonantly with the voltage pulse driven on Strip 4 and explains the observed gain.
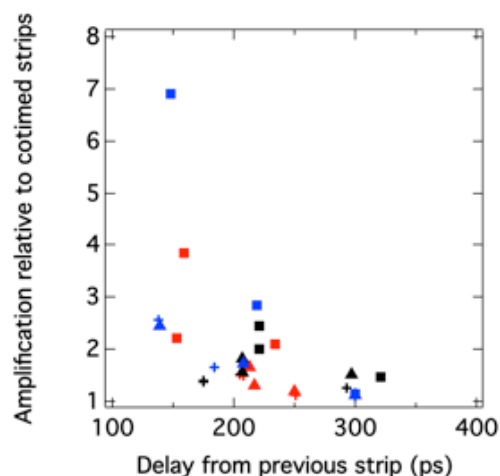

Figure 23: *Gain variation with interstrip timing for several framing camera configurations. Gain amplification due to timing variations is plotted versus observed time between one strip and its nearest neighbor. Gain variations are large when interstrip timing is less than 250 ps. Data is presented for three cameras, which are each represented by a different color. Different symbols represent the different strips.*

We show a set of similar data for three different cameras and a variety of timing and bias voltage configurations in Figure 23. Here we define relative gain variation in any strip (*Strip i*) due to interstrip timing *(t)* as the gain relative to a reference strip (Strip 1) normalized by the gain relative to that reference strip
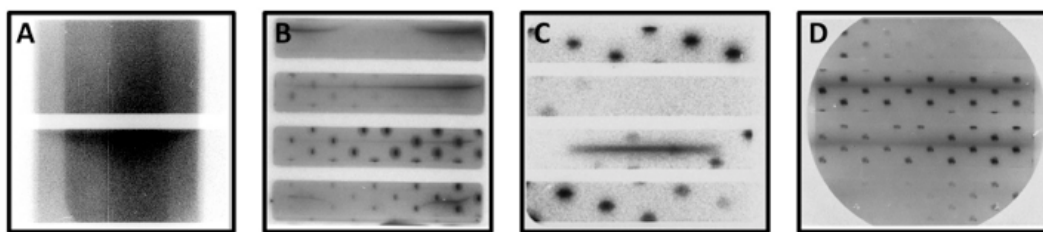
Figure 24: *Images of early light artifact as observed on four different framing cameras. Note that the location and intensity variations of the artifact are different for each camera.*

when the delay between strips is 0. That is: $G_{rel}(t)=[(G_{i,t}/G_{1,t})/(G_{i,0}/G_{1,0})]$. Strip 1 is used as the reference in this calculation because it is pulsed first and, consequently, does not receive voltage from strips that are pulsed afterward. However, if voltage is transferred from Strip 1 to Strip 2 (for example), it is not strictly true that the gain in Strip 1 is unaffected and the gain in Strip 2 is enhanced. Rather, the gain in Strip 1 is commensurately reduced in order to amplify the gain in Strip 2. However, absolute gains are difficult to measure precisely, so we use gain relative to Strip 1 as a consistent relative value.

We see in Figure 23 that as interstrip delay is decreased (and voltage pulses are able to interact), gain amplification and variation are increased.

III. Advance radiation artifacts

Radiation that arrives before a framing camera is triggered can cause an artifact

A spatially varying background signal has been increasingly observed on data collected at NIF (Figure 24). The artificial signal often appears as a background intensity that is higher along the rough center of each microstrip than along the edges of the microstrip. However, the precise location of the artificial signal is different for each individual framing camera. Artifacts are typically not present on the first strip that is pulsed.

Observation of the artifact is linked to indirect-drive ICF implosions and not to most other types of experiments. In these experiments, a plastic-coated capsule is imploded by a nearly-spherically symmetric ablation by x-rays created by a long-duration (10–20 ns) laser pulse incident on the walls of a gold hohlraum surrounding the target capsule [14]. When the capsule reaches peak compression (often ~1 ns after peak drive), the imploding core is at high density/high temperature and emits x rays. These self-emission x rays are then collected with x-ray imaging diagnostics (x-ray framing cameras) to determine the size and symmetry of the hot imploding material and stagnating core [7].

During the time that the laser is driving ablation and implosion, soft x rays are emitted from the hot *hohlraum* walls and are incident on the MCP of the x-ray framing camera. These x-rays that arrive before the camera is triggered were not thought to have any effect on the images collected at later times because the voltage on the MCP was not sufficient to amplify any electrons liberated by the high-energy photons.

In contrast, careful mining of the NIF archive indicates that both the intensity and shape of the artifact depend on the x-ray emission from the hohlraum during the drive phase. Specifically, the artifact intensity increases with total drive emission, and the shape of the artifact narrows as the time between peak drive emission and camera trigger increases. In addition, the artifact signal is more intense when higher bias voltages are used to reduce the framing camera gain. We also find that the location of any artifact is different for each minor modification in framing camera head (architecture) design. Together, these observations suggest that the artifact is created
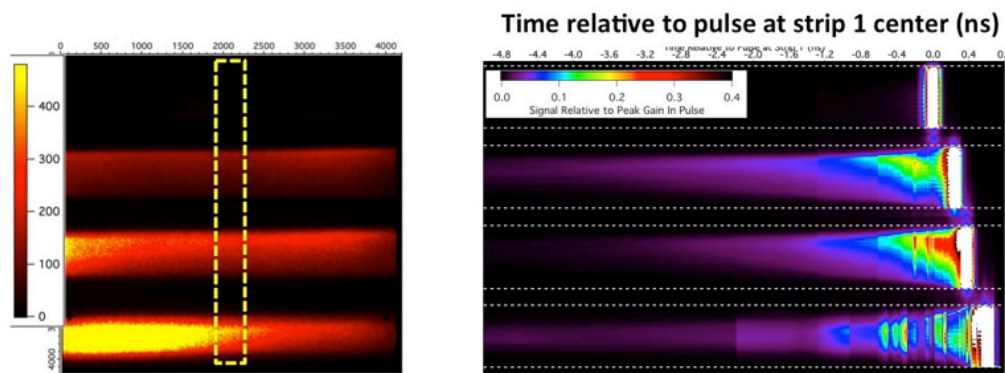
Figure 25: *Evidence of artifact in gate profile data. (Left) A single image triggered 1 ns after illumination with a short-pulse laser showing artificial signal >100 CCD counts above background. (Right) A compilation of several dozen images collected at different trigger times. Relative signals in each strip are normalized to the peak intensity of the gain pulse on that strip.*

by the interaction of incident x rays with the electric field that is present at the MCP surface before the camera is triggered.

Experiments confirm that the artifact is caused by advance photons

We established that light arriving before the voltage pulse can cause an artificial signal using the gate profile technique described above. While the gate profile is normally used to determine qualities of the voltage/gain pulse itself, we found that we could produce an artifact quite similar to those observed at NIF by triggering the camera at times after the laser arrived at the MCP.

The image on the left of Figure 24 is a single framing camera exposure collected when the ultraviolet (UV) laser arrived at the MCP 1 ns before the voltage pulse arrived in the center of Strip 1. In this experiment, each strip of a four-strip framing camera (from top to bottom) was triggered 200 ps after the strip before it—a common experimental configuration that allows for an 800 ps, continuous record of images. In this configuration, signal was produced on strips 2, 3, and 4 despite lacking any incident light when they were triggered. The color scale on the left (yellow is hot) is in background-subtracted CCD counts. Signals as high as a few hundred counts above background were observed, a not-insignificant fraction of the ~10,000 counts that comprise

the linear range of the camera and roughly 10% of the peak signal often observed.

We collected similar images over a period of time from 4 ns before the first strip was triggered to 1 ns after the final strip was triggered and at intervals of ~100 ps (images collected when gain was present comprise the gate profile data; they were collected at shorter intervals in order to characterize the gate profile accurately). We combine the result of similarly collected images at different times in the right image of Figure 25. In order to compare images, the signal at the center of the MCP (outlined by the dashed yellow box on the left) is averaged and then plotted on the right hand in Figure 25. Observed signal in each strip is plotted versus time relative to the arrival of the voltage pulse on the first strip. For consistency of color scale, intensity is normalized to 1 at the peak gain in each strip.

We find that there is a persistent artifact for at least 4 ns before the pulse arrives. The magnitude of the artifact increases continuously as the illumination time approaches the time that the gain pulse reaches Strip 1, reaching values as high as 30% of the peak gain. The location of the peak artifact signal also varies, with the signal more narrowly located on the MCP for longer delays between illumination and amplification. This characteristic is consistent with our findings in the archive of NIF data.

Because the short-pulse laser source is much shorter than the framing camera gate, the result
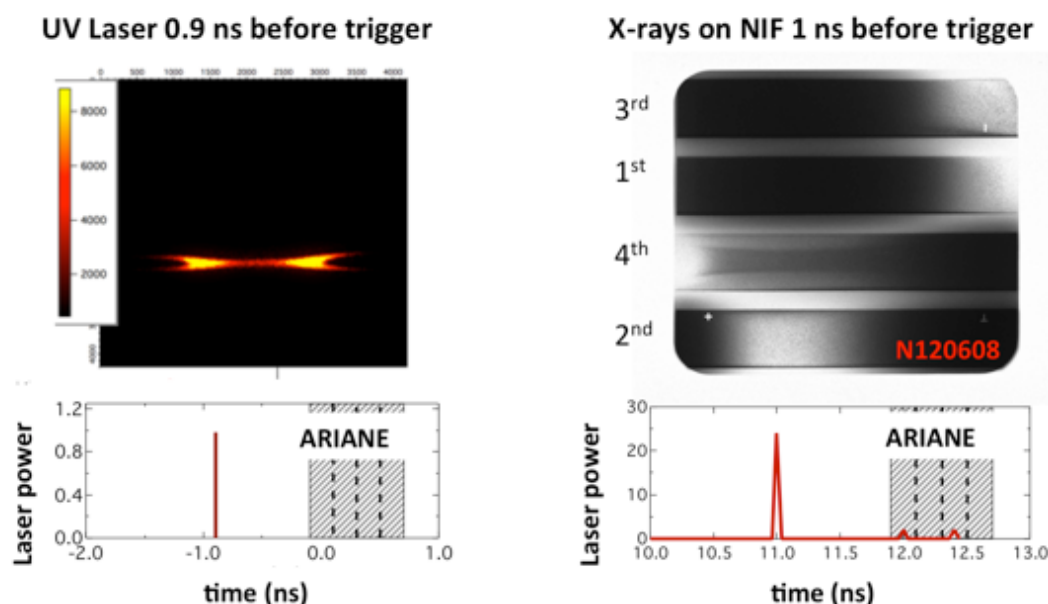
Figure 26: *(Left) Artifact produced by a <1 ps ultraviolet (UV) laser on the ARIANE [15] framing camera. (Right) Artifact produced at ARIANE by x rays from an 88 ps laser impulse onto a gold sphere. In both cases, the pre-illumination occurred over a very short time, and a distinctively shaped artifact was produced.*

in Figure 25 represents a nearly instantaneous response to advance x rays. The total observed artifact in any experimental situation would be effectively predicted by the integral of the relative x-ray emission—rather than a single short-pulse lab image—at each time before the camera is triggered multiplied by the artifact produced at that relative time.

However, in one experiment at NIF—a diagnostic timing shot in which we were using laser impulses on a gold sphere to produce x rays and to time multiple instruments—we unintentionally reproduced the conditions in the short-pulse laser lab, providing further confirmation that the signal produced by pre-illuminating the framing camera with the UV laser could also be produced by high-energy x rays. In this case, an 88 ps laser impulse was applied ~1 ns before the framing camera was triggered in order to time a different instrument [11]. In addition to the timing signal expected on the ARIANE [15] framing camera, an artifact was present on a strip of the framing camera that otherwise received no signal (Figure 26). The distinctive shape of the artifact, shown on the right side of Figure 26, was very similar to the shape observed in the short-pulse

lab, which is shown in the left side of Figure 26. When longer ICF/hohlraum signals are present in advance, the artifact on that same framing camera was more diffuse (Figure 24c).

Thus, we have linked advance UV impulses to distinctive, spatially varying signals. We have also linked the signal due to a single advance UV impulse to an advance x-ray pulse of a slightly longer timescale (88 ps). This comparison bolsters the idea that as the advance signal duration increases, the total artifact signal may become more broad or diffuse in a way that is consistent with the temporal integral of the advance x-ray intensity due to the impulsively produced signals that can be measured with the gate profile method.

Simulations confirm that the electric field is sufficient to trap electrons

The physical mechanism that has thus emerged to describe the observations is this: high-energy photons that arrive in advance of the trigger hit the MCP and liberate one or more electrons. This process happens any time a photon is incident on the MCP unless charge is depleted for some reason. While one might have expected any early electrons to
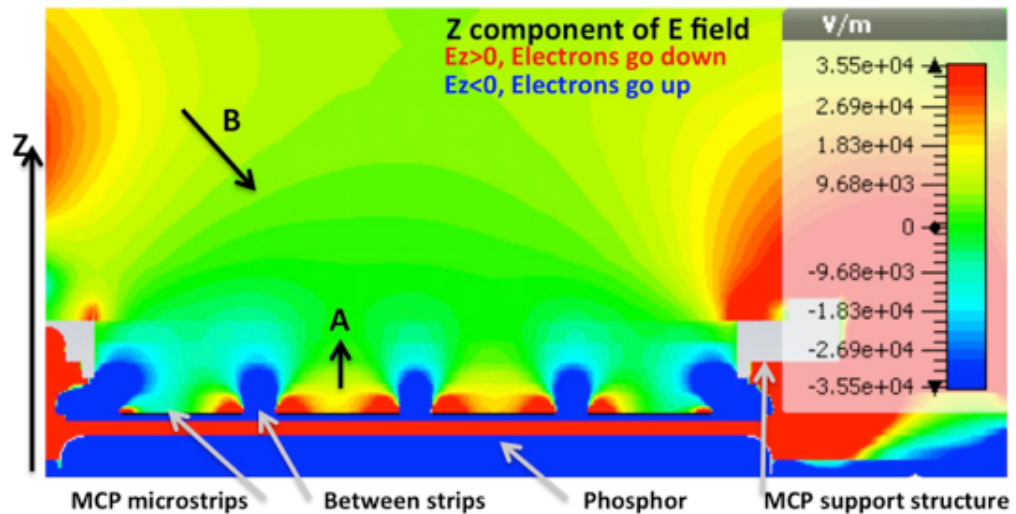
Figure 27: *Static calculation of electric field in four-strip framing camera head with +450 V DC bias on the MCP and +5 kV quasi-static voltage on the phosphor. The specific geometry of the microchannel plate (MCP) support structure and framing camera housing (in this case non-magnetic PEEK) are identical to the as-built geometry of the ARIANE camera [15]. Variations in the DC bias change the region of negative Ez above the individual microstrips (marked A), while variations in the voltage on the phosphor change the location of the equipotential surface above the head (marked B).*

dissipate by either leaving the MCP surface or being reabsorbed, it appears that some are trapped at the surface of the MCP. As a result, when the voltage pulse passes at a later time, those trapped electrons are amplified, producing additional background signal.

The electrons that are trapped at the surface are not uniformly distributed, but instead appear to produce additional background signals at preferred locations. Because electrons respond via the Lorentz force to any static electric field present before the pulsed voltage arrives, this suggests that there is a non-uniform electrostatic field with preferred low potential regions. The reduced artifact at long delays suggest that some electrons *are* dissipating, but on a timescale that is greater than ~1 ns. Still, the continued presence of a small artifact at times as early as 4 ns (or more) suggests that some electrons are effectively trapped.

We reinforce many elements of this hypothesis with a suite of simulations. The calculations and results of our electrostatic, full-wave electromagnetic, and particle-in-cell simulations have been described in somewhat greater detail in [16 and 17]. An

example of the electrostatic field calculation for a four-strip framing camera is shown in Figure 27. The vertical component of the field is plotted on a color scale in which positive electric fields are red, and negative electric fields are blue. Electrons that are at or above the MCP surface are accelerated upward (away from the MCP) when $E_z<0$ *(blue)*, and they are accelerated downward (toward the MCP, or trapped) when *Ez>0 (red)*.

In this simulation we find that there are regions at the edge of each microstrip where electrons are strongly attracted to the MCP surface and that the entire surface of the two central microstrips attracts electrons. As the positive bias voltage on the microstrips is increased, the positive (trapping) field is also increased.

The entire assembly contributes to the static field at the MCP surface to a surprising degree. In order to accurately reproduce the observed artifacts, we found that it was necessary to include the specific architecture of the entire head rather than merely the local region just above the microchannel plate. In addition to the MCP surface and the ground-plane at the back of the MCP, this architecture included
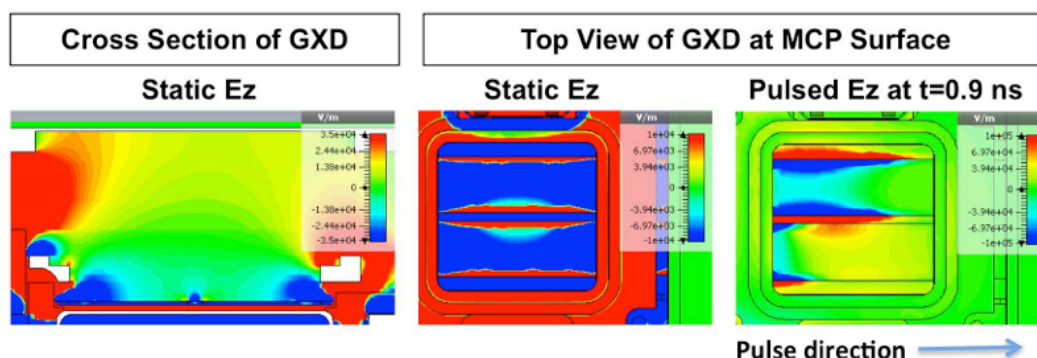
Figure 28: *Electric field due to static +100 V bias voltage (left, middle) and -1 kV Gaussian voltage pulse, 200 ps full width at half-maximum (FWHM) (right).*

the high-voltage surface of the phosphor, the supporting structures holding the MCP in place (which are not grounded and thus float to hold potential), and even the camera housing, which is composed of metal or non-metallic PEEK.

When the entire geometry is accounted for, the high voltage at the phosphor is strong enough to "leak" around the MCP to create a positive electric field above the MCP surface. This field is asymmetric due to the cabling that brings voltage to the phosphor, which creates a stronger field at the phosphor voltage input side.

Once the electrostatic models were sufficiently detailed to describe the static field before camera operation, we proceeded to a dynamic model that could describe the electric field at the MCP when the voltage pulse is present. Figure 28 shows an example of the electrostatic and electromagnetic wave simulations for a two-strip framing camera (HGXD). The left-hand image shows a cross-sectional view of the MCP surface as in Figure 27. The middle image shows a top view of the same calculation in a plane just above the surface of the MCP. From this image, it can be inferred that electrons might be confined at the MCP surface at the top and bottom edge of each strip. The right-most image shows the field when the voltage pulse is present. In this simulation, the pulse is timed to arrive at the center of strip 1 at t = 1 ns. At t = 0.9 ns, the pulse is peaked slightly to the left of center in strip 1.

While there is no voltage applied to the bottom strip in the right image, our simulation agrees with our previous work in finding that there is a voltage induced on the second strip that is proportional to the inverse of the time derivative of the pulse on the first strip. Thus, there is a strong positive ("trapping") voltage on Strip 2 consistent with the peak derivative of the pulse driven on Strip 1.

The pulsed simulation does not include the static bias voltage. Consequently, the total voltage on the MCP when the pulse is present is the super-position of the middle and right image in Figure 28. Thus, the most likely location for electrons to be confined at the MCP surface is at the top (and to a slightly lesser extent, the bottom) of the second strip, and this is indeed where artifacts are observed on the two-strip framing camera (see Figure 33a).

We take this idea one step further by performing time-dependent particle-in-cell simulations. In this simulation, 1×10^6 electrons are "released" just above the surface of the MCP at t = 0, and they are allowed to evolve according to their initial energy and whatever forces accelerate them. The ensemble of electrons has an initial average energy ~ 1 eV, which we believe to be a reasonable approximation for the population of electrons emitted from the MCP. As in the full-wave electromagnetic simulations, the MCP surface has a +100 V DC bias, and an additional -1 kV pulse arrives at the center of strip 1 at 1 ns.

We plot in Figure 29 the location of electrons in the plane just above the MCP (where they were released) as a function of time, and the markers that indicate electron locations are
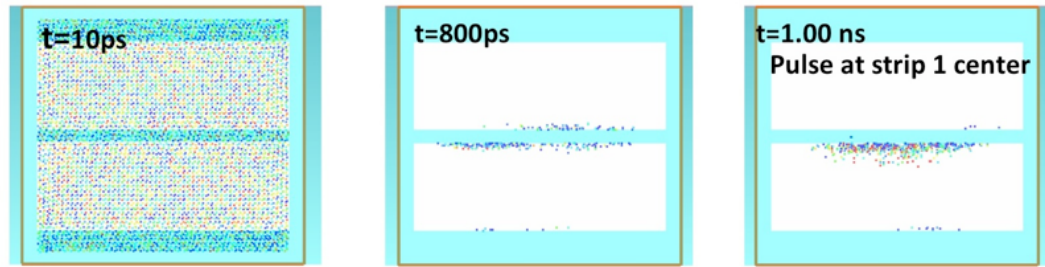
Figure 29: *Particle-in-cell simulations demonstrating that electrons are trapped at MCP surface. Electrons are released just above the MCP surface at t = 0. The MCP is held at +100 V DC until the -1 kV Gaussian voltage pulse (200 ps FWHM) arrives at t =1.0 ns. Images indicate the location of electrons, and the color of each marker indicates the energy.*

also colored to indicate energy. Just after release, electrons fill the plane above the MCP, having a broad energy distribution. After time has elapsed, fewer electrons remain in the plane, as most have begun to disperse. However, some electrons remain at the strip boundaries, consistent with the electrostatic calculations. Once the pulse arrives, we find that even more electrons are pushed back to the MCP surface at the top of Strip 2 by the electric field that is induced by the drive voltage on Strip 1.

ERASER inhibits artifacts by changing the static electric field

Armed with a physics-based understanding of the observed artifacts, we posit that they can be effectively inhibited by removing electrons from just above the surface of the microchannel plate. If a small electrostatic field can trap electrons, then we expect that electron removal can be achieved also by a change to the static electric field of the framing camera head. Thus, we designed a high-voltage surface to attract

electrons as an additional element to be added to the framing camera head. A schematic of this device (ERASER) is shown in Figure 30. This concept is a logical extension to an approach taken to increase the efficiency of MCPs used as astronomical detectors [18]. In that application, MCPs are amplified with a DC voltage because all incident photons are of interest, and no photo-electrons are unwanted. MCP detector efficiency was effectively increased by applying an electric field above the surface of the MCP that accelerated electrons *toward* the MCP, preventing any electrons from dissipating before they could be amplified.

In contrast, ERASER counteracts the small trapping field of a few hundred volts at the surface of the MCP with a more strongly positive potential surface (~ +1 kV) about 1 cm above the MCP surface. This potential surface then attracts electrons at the microstrip surface during the time before (and after) the voltage pulse is present, but it is not strong enough to attract electrons at the MCP surface when the
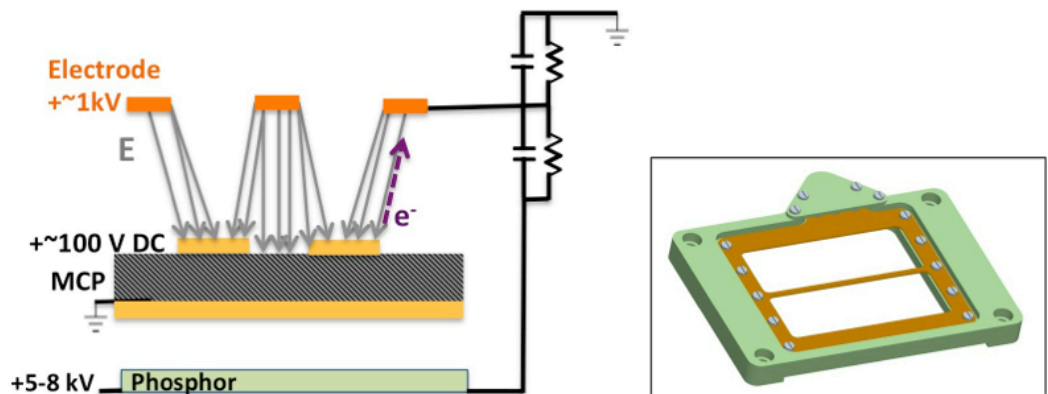

Figure 30: *Schematic diagram of early radiation artifact suppression electrode rig (ERASER).*
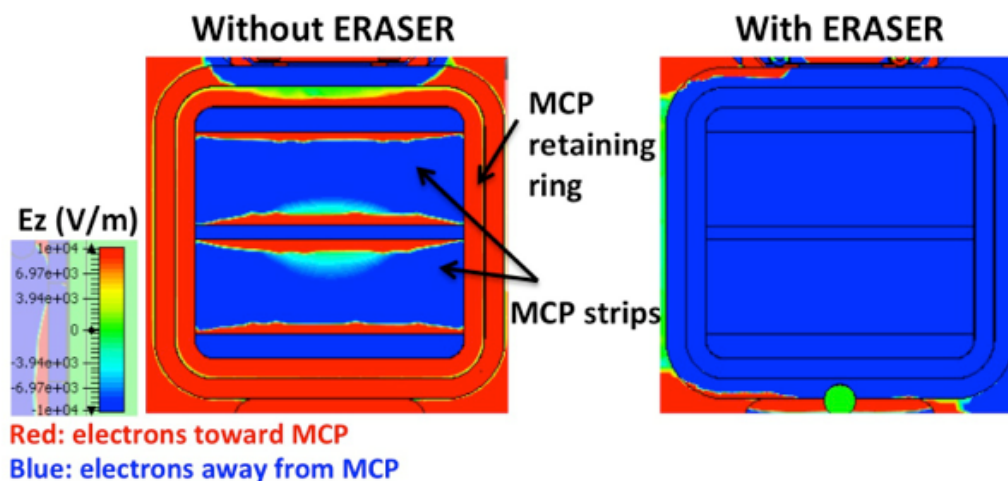
Figure 31: *Static E$_z$ determined by 3D modeling at times before the camera is triggered is plotted on a top-down view of the MCP to show spatial variation of the electrostatic field across the microstrips. (Left) Without the ERASER to attract early electrons, positive values of E$_z$ can act to trap electrons. (Right) With the ERASER, static electric fields at the surface of the MCP are uniformly negative, accelerating any electrons created before the camera is triggered away from the MCP.*

driving voltage pulse (~ -1 kV) is present. The electrode is shaped complementarily to the geometry of the microstrips—it is only present above the spaces between microstrips in order to not interfere with incident x-rays when the camera is triggered. The voltage is provided by the same circuit that powers the phosphor [19].

We added this design for ERASER to the models that were used in the simulations described above and found that this design did change the static electric field at the MCP surface. Once the ERASER is added, there is no trapping field at the MCP surface. The electrostatic field is repulsive everywhere (Figure 31).

We also reran the particle-in-cell (PIC) simulations with ERASER present, and the results are shown in Figure 32. Here, however, we show a cross-sectional view of the framing camera head, and we plot the location and energy of electrons 1 ns after they are released. Without ERASER present, most electrons have traveled only a short distance from the MCP surface, but with ERASER present, the electrons are accelerated upwards, traveling faster and moving farther away.

Our first ERASER was built for a two-strip framing camera (HGXD3), and it was tested with the gate profile method (as in Figure 25,

images were collected starting 4 ns before the gain pulse arrived in the center of the first strip). Images in the top of Figure 33 are similar to Figure 25, showing the shape, intensity, and delay response of the early-light artifact for this camera. Figure 33a indicates that the artifact is very similar to the shape/geometry of the attracting electrostatic field in Figure 28
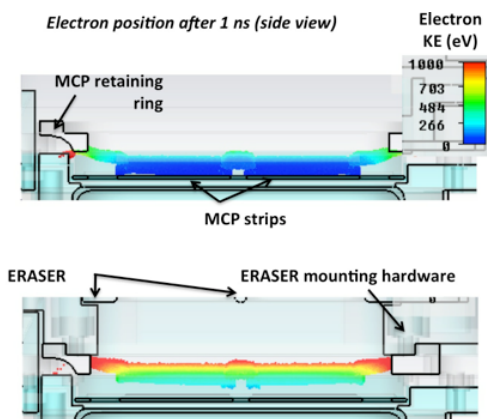

Figure 32: *Location and energy of electrons released at the surface of the MCP after 1.0 ns. (Top) Without the ERASER to attract early electrons, many electrons remain close to the surface of the MCP. (Bottom) With the ERASER, electrons are accelerated away from the MCP. They are farther away after 1 ns, and they are travelling faster.*
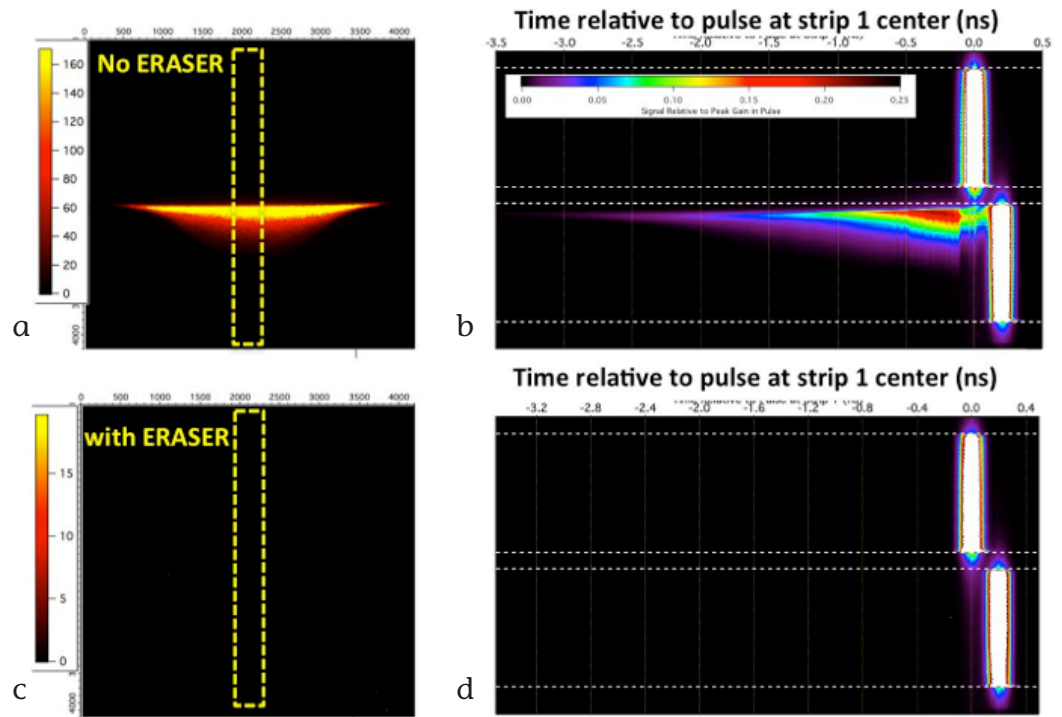
Figure 33: *(a) Image collected on a two-strip framing camera illuminated by a UV laser 1.0 ns before the camera was triggered. Strip 2 is delayed 200 ps relative to strip 1. (b) Evolution of the artifact with the delay between UV laser illumination and camera trigger. Data was processed as described in the caption to Figure 8. Bottom images are identical to the top images except that a high-voltage electrode (ERASER) was added.*

and Figure 31 and to the electrons trapped by PIC simulations in Figure 29.

In contrast, once ERASER is added to the framing camera head (bottom images in Figure 33), no artifact is observable with the extended-time gate profile measurements. In addition, we took advantage of the fact that we can also measure relative gains with the gate profile method. By using the same optical filter setup for both measurements and carefully using identically collected flat-field data, we could confirm that the framing camera gain when ERASER is present is within 5–10% of the gain before ERASER was installed.

The definitive demonstration that ERASER effectively inhibits artifacts in the NIF application—where advance radiation may be more intense and is certainly more temporally extended. In January 2014, two new framing cameras were installed at NIF. These two cameras with ERASER, one two-strip (HGXD3) and one four-strip (HGXD2), are film-based for high-neutron-yield applications.

Figure 34 shows implosion image data from similar implosions on two four-strip, film-based framing cameras. In the image on the left, which was collected with a camera that did not have ERASER (HGXI-1) [20], substantial artifacts are seen on the second and third strips. In contrast, the image on the right, which was collected with a framing camera that does have an ERASER attachment (HGXD2), there is no evidence of any artifact, despite the high-power holhraum drive (410 TW for 3 ns, ending less than 1 ns before the framing camera was triggered).

Indeed, no artifacts have been observed on any camera with ERASER, though they continue to be observed on the existing fleet of framing cameras without ERASER. The NIF framing-camera engineering team plans to install ERASER on all new framing cameras, and as time permits, to retrofit the current fleet of framing cameras with an ERASER attachment.
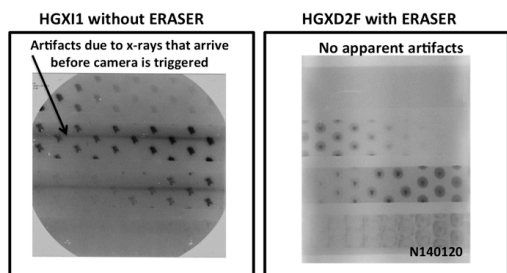
HGXI1 without ERASER — Artifacts due to x-rays that arrive before camera is triggered

HGXD2F with ERASER — No apparent artifacts — N140120

Figure 34: *ERASER inhibits artifacts due to advance radiation.*

IV. Conclusions

Here we have described and purposely linked the observations of electromagnetic crosstalk and early-radiation artifacts in x-ray framing camera data. We have found that these two phenomena can have a strong effect on framing camera performance and can lead to significant challenges in quantitative analysis of x-ray images. Both phenomena also require a sophisticated knowledge of framing camera operation to understand and depend strongly on components of the framing camera that were otherwise not expected to contribute to performance.

Nonetheless, at NIF we have made significant progress toward characterizing, modeling, and most importantly, minimizing both of these effects. We also continue to apply this understanding to our designs of future framing cameras, emphasizing robust crosstalk and early radiation.

V. Acknowledgments

VI. References

[1] J.D. Kilkenny, "High Speed Proximity Focused X-ray Cameras," *Laser and Particle Beams*, **9**(1), 49 (1991).

[2] B.F.K. Young et al., "Experiment demonstration of a 100ps microchannel plate framing camera," *Rev. Sci. Instrum.*, **57**, 2729 (1986).

[3] K.S. Budil et al., "The Flexible X-ray Imager," *Rev. Sci. Instrum.*, **67**, 485 (1996).

[4] J.A. Oertel et al., "Gated X-ray Detector for the National Ignition Facility," *Rev. Sci. Instrum.* **77**, 10E308 (2006).

[5] J.R. Kimbrough et al. "Standard design for National Ignition Facility x-ray streak and framing cameras," *Rev. Sci. Instrum.* **81**,10E530 (2010).

[6] D.R. Hargrove, J.P. Holder, N. Izumi, L.R. Benedetti, G. Stone, J. Kimbrough, P.M. Bell, and S. Glenn, "NIF's Hardened Gated X–ray Detector, hGXD," *Proc. SPIE 2014* (in press).

[7] S.M. Glenn et al., "Extracting core shape from x-ray images at the National Ignition Facility," *Rev. Sci. Instrum.* **83**, 10E519 (2012); doi: 10.1063/1.4731743.

[8] C.A. Kruschwitz et al., "Monte Carlo simulations of microchannel plate detectors. II. Pulsed voltage results," *Rev. Sci. Instrum.* **82**, 023102 (2011).

[9] S.F. Khan et al., "Methods for characterizing x-ray detectors for use at the National Ignition Facility," *Rev. Sci. Instrum.* **83**, 10E118 (2012); doi: 10.1063/1.4731743.

[10] E.L. Dewald et al., "Dante soft x-ray power diagnostic for National Ignition Facility," *Rev. Sci. Instrum.* **75**, 3759 (2004).

[11] S.F. Khan et al., "Measuring x-ray burn history with the Streaked Polar Instrumentation for Diagnosing Energetic Radiation (SPIDER) at the National Ignition Facility (NIF)" *Proc. SPIE* **8505**, 850505 (2012); doi:10.1117/12.930032.

[12] J.A. Oertel and T.N. Archuleta, "A novel solution to the gated x-ray detector gain droop problem," *Rev. Sci. Instrum.* (in press).

[13] L.R. Benedetti et al., "Crosstalk in x-ray framing cameras: Effect on voltage, gain, and timing," *Rev. Sci. Instrum.* **83**, 10E135 (2012); doi: 10.1063/1.4740524.

[14] J.D. Lindl et al., "The physics basis for ignition using indirect-drive targets on the National Ignition Facility," *Physics of Plasmas* **11**(2), 339 (2004).

[15] M.J. Ayers et al., "Design and Implementation of Magnification Framing Camera for NIF ARIANE Light," *Proc. SPIE* **8505**, 85050J (2012).

[16] M.P. Perkins et al., "Computational studies of X-ray framing cameras for the National Ignition Facility," in *Pulsed Power Conference*, 2013 19th IEEE (2013) pp. 1, 6, 16–21; doi: 10.1109/PPC.2013.6627632.

[17] L.R. Benedetti et al., "Investigation and suppression of artifacts in x-ray framing cameras due to advance radiation incident on microchannel plates," *Proc. SPIE* **8850**, 88500J (2013); doi: 10.1117/12.2027149.

[18] R.C. Taylor et al., "Maximizing the Quantum Efficiency of Microchannel Plate Detectors: The Collection of Photoelectrons from the Interchannel Web using an Electric Field," *Rev. Sci. Instrum.* **54**(2), 171 (1983).

[19] C.S. Anderson et al., "P-Spice Modeling of Attractor Grid Voltage for Implementation in NIF GXD Framing Cameras," LLNL-TR (2013).

[20] S. Glenn et al., "A hardened gated x-ray imaging diagnostic for inertial confinement fusion experiments at the National Ignition Facility," *Rev. Sci. Instrum.* **81**, 10E539 (2010); doi: 10.1063/1.3478897.

NIF

lasers.llnl.gov